Soil Dynamics and Earthquake Engineering 108 (2018) 111–129

Contents lists available at ScienceDirect

Soil Dynamics and Earthquake Engineering

journal homepage: www.elsevier.com/locate/soildyn

# Seismic demand of base-isolated irregular structures subjected to pulse-type earthquakes

Fabio Mazza

*Dipartimento di Ingegneria Civile, Università della Calabria, Rende, Cosenza, Italy*

ARTICLE INFO

*Keywords:*
Pulse-type earthquake
Forward-directivity effect
Near-fault area
Wavelet analysis
Fixed-base irregular structures
Retrofitted base-isolated structures
Elastomeric and sliding bearings
Nonlinear dynamic analysis

ABSTRACT

Base-isolated structures may be subjected to severe seismic demand in the superstructure and/or in the isolation system at sites located near an active fault. Forward directivity effects with long-period horizontal pulses in the fault-normal velocity signals are the main cause of this behaviour. However, recent studies have identified pulses in arbitrary orientations along with false-positive classification of pulse-type ground motions. The aim of the present work is to evaluate the reliability of elastomeric (i.e. high-damping-laminated-rubber bearings, HDLRBs) and sliding (i.e. curved surface sliding bearings, CSSBs) base-isolation systems for the seismic retrofitting of in-plan irregular buildings located in the near-fault area. To this end, a five-storey reinforced concrete (r.c.) framed structure, with an asymmetric-plan and bays of different length, is chosen from benchmark structures of the Re.L.U.I.S. project. Attention is focused on the pulse-type and non-pulse-type nature of near-fault earthquakes and moderately-soft and soft subsoil conditions. First, a comparison between algorithms based on wavelet signal processing, that can identify pulses at a single (e.g. fault-normal) or arbitrary orientation in multicomponent near-fault ground motions, is carried out to classify records of recent events in central Italy and worldwide. Then, nonlinear seismic analysis of the fixed-base and base-isolated test structures is performed by using a lumped plasticity model to describe the inelastic behaviour of the r.c. frame members. Nonlinear force-displacement laws are considered for the HDLRBs and CSSBs, including coupled bi-directional motions in the horizontal directions and coupling of vertical and horizontal motions.

## 1. Introduction

First the detrimental effects of pulse-type near-fault ground motions on structural response are recognized in [1–4]. Next, near-fault ground motions worldwide (e.g. Chi-Chi in Taiwan, Northridge in U.S.A. and Kobe in Japan to name a few) exhibiting high-amplitude and long-period velocity pulses raise concerns about the reliability of the base-isolation as control system of existing framed buildings [5–8]. Amplification in the inelastic demand of the superstructure and large displacement at the base are generally expected for base-isolated structures located in the near-fault area [9,10], making it difficult and expensive to design optimal solutions [11,12]. In particular, forward directivity effects tend be maximum along the fault-normal direction, referring to the horizontal ground-motion components [13], although pulse-type earthquakes are also observed in different orientations [14]. However, not all near-fault ground motions experience pulse-type effects along with false-negative classifications that can occur when only one potential pulse is considered [14–16]. Moreover, the pulses caused by directivity effects arrive early in the velocity time history but pulse-type ground motions can be also caused by soft-soil effects. Finally, seismic sequences in near-fault area recorded during recent earthquakes in central Italy (i.e. L'Aquila in 2009 and Rieti in 2016) focus attention on the residual deformations of r.c. framed structures [17–19], giving rise to an interest in the retrofitting of existing structures with base-isolation systems to limit the accumulation of damage.

Coupled torsional-translational response of asymmetric-plan framed buildings adversely affects the nonlinear seismic behaviour, which results in irregular concentration of inelastic demand leading to structural collapse. Base-isolation is generally considered an effective means of reducing asymmetry if the stiffness (CS) and strength (CST) centres of the isolation system are directly under the centre of mass (CM) of the superstructure [20,21]. Significant sources of torsional motions in elastomeric [22] and sliding [23] base-isolated structures are the stiffness eccentricity (i.e. the distance between CS and CM) and the lateral and torsional flexibility of the superstructure. Mass-eccentric rather than stiffness-eccentric superstructures produce torsional amplifications [24], while an eccentric isolation system may adversely affect its effectiveness since the maximum displacement is increased [25]. Moreover, the maximum amplification of the response occurs at the stiff or flexible edge for torsionally flexible or rigid base-isolation systems,

*E-mail address:* fabio.mazza@unical.it.

https://doi.org/10.1016/j.soildyn.2017.11.030
Received 8 August 2017; Received in revised form 26 November 2017; Accepted 27 November 2017

respectively [26]. Finally, by observing the nonlinear behaviour of the superstructure one founds that CS ≡ CST ≡ CM is convenient only for accommodating torsional effects in the base isolation system but might cause more damage in the flexible side of the superstructure [27]. On the other hand, elastomeric and sliding bearings may suffer from tension or uplift, respectively, accompanied by large horizontal shear strain under violent near-fault earthquakes. Specifically, overturning moments during seismic excitation can induce undesirable tensile forces in elastomeric bearings [28,29] or uplift in sliding bearings [8,30], which are amplified when the height-width ratio of the superstructure is large or in-plan irregularity is considered.

Although the study of the retrofit of plan-irregular buildings with base isolation is not new [31,32], this discussion emphasizes the advisability of additional studies to clear up any misunderstanding and evaluate whether a base-isolation system may also be viable for the seismic retrofitting in the near-field area, also considering in plan-irregularities inducing torsional and overturning effects. With this aim in mind, a simulation is conducted in which a five-storey reinforced concrete (r.c.) framed structure, characterized by an L-shaped plan with bays of different length, is retrofitted by insertion of an isolation system at the base for attaining performance levels imposed by current Italian code (NTC08, [33]) in a high-risk seismic zone. Specifically, elastomeric (i.e. Elastomeric Base-Isolated, EBI, structure with high-damping-laminated-rubber bearings, HDLRBs) and sliding (i.e. Sliding Base-Isolated, SBI, structure with curved-surface-sliding bearings, CSSBs) base-isolation systems are considered. Four test structures are considered for each base-isolation system, considering: design seismic loads constituted of the horizontal component acting alone or in combination with the vertical one; subsoil classes C and D, corresponding to moderately soft- and soft-site, in accordance with the NTC08 classification. A comparison of the 3D nonlinear dynamic analysis for the original fixed-base (FB) and retrofitted base-isolated (EBI and SBI) structures subjected to near-fault earthquakes is presented. An algorithm based on the wavelet transform of a single component [13], typically the fault-normal orientation, or two orthogonal components [14] is adopted to classify near-fault ground motions as pulse-type or non-pulse-type in the horizontal direction. Next, 3D model of the fixed-base and base-isolated structures subjected to the horizontal and vertical components of near-fault earthquakes is considered. To this end, records of recent earthquakes in central Italy [34] and worldwide [35] are selected from the Italian Accelerometric Archive (ITACA) and the Pacific Earthquake Engineering Research (PEER) centre Next Generation Attenuation (NGA) database. To minimize the variability in the prediction of response parameters, a modified velocity spectrum intensity measure is evaluated and the selected earthquakes scaled in line with the NTC08 design spectra.

## 2. Pulse-type indicators for near-fault earthquakes

Pulse-type near-source ground motions may be the result of forward directivity effects, which result in a double-sided velocity pulse at the beginning of the time-history whose duration is expected to scale with magnitude [36]. This happens because seismic waves generated at different points along the rupture front arrive at a site at the same time when the fault rupture propagates towards the site and the slip direction is aligned with the site [37]. Evidence of impulsive features in near-source area are identified in recent earthquakes in L'Aquila (April 6th, 2009) and Rieti (August 24th, 2016) and their seismic sequences [13,18,19,38]. Elsewhere, rupture directivity effects can be also found in many worldwide strong near-fault records: e.g. Taiwan (Chi-Chi, September 20th, 1999), California (Northrdige, January 17th, 1999) and Japan (Kobe, January 16th, 1999). Leaving aside visually classified pulses, a broad algorithm used to classify these ground motions as pulse-type is based on wavelet analysis, by examining a single component of the original velocity time-history (typically that in the fault-normal orientation) to identify and extract the pulse, evaluating its period ($T_P$) and the residual motion after the pulse is removed [14]. A pulse indicator (i.e. a dimensionless real number PI varying in the range 0–1) is evaluated

$$PI = (1 + e^{-23.3+14.6(PGV\ ratio)+20.5(Energy\ ratio)})^{-1} \quad (1)$$

which is function of amplitude and energy of the residual and original (recorded) ground motions

$$PGVratio = \frac{PGV_{residual\ \ record}}{PGV_{original\ \ record}},\ Energy\ ratio = \frac{CSV\,(t_{tot})_{residual\ \ record}}{CSV\,(t_{tot})_{original\ \ record}} \quad (2a,b)$$

where the energy can be computed as the cumulative squared velocity of the signal during the total duration of the earthquake ($t_{tot}$)

$$CSV\,(t_{tot}) = \int_0^{t_{tot}} V^2(\tau)d\tau \quad (3)$$

In particular, a ground motion is classified as pulse-type when a PI value in excess of 0.85 is scored together with a peak ground velocity (PGV) greater than 30 cm/s. Moreover, early pulses, produced by directivity effects, are distinguished by late pulses, due to soft-soil effects, using the time at which the CSV of the extracted pulse attains 10% of its total value (i.e. $t_{10\%,pulse}$) before the original ground motion reaches 20% of its CSV (i.e. $t_{20\%,original}$). However, this algorithm fails to capture pulse-type earthquakes in orientations different from fault-normal, and it is thus unusable when the fault-normal orientation itself is unknown. To overcome these problems, the ground motion can be rotated in all orientations (i.e. 0–180°, to avoid redundancy) and it can considered as pulse-type if a pulse is identified at least in one orientation [15]. On the other hand, this approach is computationally expensive and can lead to non-pulse-type ground motions being classified as pulse-type, because the PGV threshold is assigned arbitrarily. Finally, an improved algorithm avoiding false-positive classifications finds five potential orientations that are the most likely to contain strong pulses, also introducing a modified expression of the pulse indicator [16]

$$PI = 9.384(0.76 - PC - 0.0616PGV)(PC + 6.914.\ 10^{-4}PGV - 1.072) - 6.179 \quad (4)$$

with a principal component (PC) evaluated as linear combination of the PGV and energy ratios

$$PC = 0.63.\ (PGV\ \text{ratio}) + 0.777.\ (Energy\ ratio) \quad (5)$$

The ground motion is classified as pulse-type when the PI value is positive and as non-pulse-type if negative. Moreover, the early pulses present $t_{5\%,pulse}$ greater than $t_{17\%,original}$.

Eleven recent near-fault ground motions in central Italy are selected from the Italian Accelerometric Archive [34]; recordings from ground motions with magnitude ($M_w$) between 5.9 and 6.5 and short epicentral distance ($\Delta_1$) are considered. Worldwide, three strong near-fault earthquakes, with $6.7 \le M_w \le 7.6$ and closest fault distance ($\Delta_2$), are selected from the Pacific Earthquake Engineering Research (PEER) centre Next Generation Attenuation (NGA) database [35]. The main data of the selected earthquakes (EQs) are shown in Tables 1a and 1b, respectively: i.e. earthquake, recording station, peak ground acceleration in the horizontal ($PGA_{H1}$ and $PGA_{H2}$) and vertical ($PGA_V$) directions, maximum peak ground velocity ($PGV_{H,max}$) and displacement ($PGD_{H,max}$) in the horizontal direction. It should be noted that the Accumoli and Ussita EQs are also considered in the numerical study, although Baker's original classification [14] excludes these low-amplitude records because their $PGV_{H,max}$ value is less than 30 cm/s.

Firstly, the algorithm suggested by Shahi and Baker [14,15] is implemented at different orientations of the horizontal components of the selected earthquakes in the range 0–360°, with a constant step of 10°, using Eqs. 1–3 to evaluate the PI values for the Italian (Fig. 1) and worldwide (Fig. 2) EQs. The PI threshold (i.e. 0.85) is also reported in Figs. 1 and 2 with a dashed black line. As can be observed, Italian pulse-type ground motions occur in a range of orientations for all recording

**Table 1a**
Near-fault earthquakes in central Italy (ITACA database [34]).

| *Earthquake (EQ)* | *Recording station* | $\Delta_1$ (km) | $PGA_{H1}$ (m/s$^2$) | $PGA_{H2}$ (m/s$^2$) | $PGA_V$ (m/s$^2$) | $PGV_{H,max}$ (cm/s) | $PGD_{H,max}$ (cm) |
|---|---|---|---|---|---|---|---|
| L'Aquila, 6/4/2009 ($M_w$ = 6.3) | AQA | 5.01 | 3.95 | 4.34 | 4.35 | 31.92 | 5.43 |
| | AQK | 1.76 | 3.24 | 3.47 | 3.55 | 35.80 | 11.64 |
| | AQV | 4.92 | 5.35 | 6.44 | 4.87 | 42.72 | 6.79 |
| | AQG | 4.98 | 4.37 | 4.79 | 2.35 | 35.76 | 6.00 |
| Accumoli (Rieti), 24/8/2016 ($M_w$ = 6.0) | AMT | 8.50 | 4.25 | 1.83 | 1.94 | 21.52 | 4.25 |
| | NOR | 15.60 | 3.53 | 3.66 | 2.11 | 27.04 | 7.30 |
| | NRC | 15.30 | 1.77 | 1.98 | 2.44 | 29.75 | 6.62 |
| | FEMA | 32.90 | 1.86 | 2.42 | 0.79 | 14.46 | 3.14 |
| Ussita (Rieti), 26/10/2016 ($M_w$ = 5.9) | NOR | 13.30 | 2.11 | 1.18 | 1.03 | 20.31 | 3.01 |
| Norcia (Rieti), 30/10/2016 ($M_w$ = 6.5) | FCC | 11.70 | 9.38 | 8.45 | 9.23 | 77.28 | 14.65 |
| | NOR | 5.50 | 3.04 | 2.86 | 2.79 | 56.25 | 23.05 |

stations of the L'Aquila (Fig. 1a), Accumoli (Fig. 1b) and Ussita (Fig. 1c) EQs while the Norcia site is deemed to have experienced non-pulse-type records (Fig. 1d). On the other hand, the Taiwan (Fig. 2a) and Northridge (Fig. 2b) EQs are characterized by impulsive nature in a multitude of orientations, unlike the Kobe EQ (Fig. 2c) where pulses fall within a narrow range of orientations. Moreover, polar plots highlight pulses around the fault-normal (FN) orientation for the L'Aquila and Accumoli EQs (Fig. 1a, b), while the FN orientation does not lie in the range in which pulses are observed for the Ussita EQ (Fig. 1c). Similarly, in the Kobe EQ the pulses are predominately perpendicular to the fault (Fig. 2c), contrary to the Taiwan and Northridge EQs where pulses deviate from the strictly FN orientation (Fig. 2a, b). These results confirm that false-negative classifications can occur when only one potential pulse (e.g. normal faulting type) is adopted for the classification of the behaviour of near-source ground motions.

Next, the improved pulse classification algorithm proposed by Shahi and Baker [16] is used to classify up to five potential pulses for each ground motion. Main results are reported in Tables 2a and 2b for each potential pulse of the selected EQs in Italy and worldwide, respectively: i.e. angle of orientation ($\alpha$) in the clockwise direction from North, pulse period ($T_P$), pulse indicator (PI) evaluated in line with Eqs. 4 and 5. It is interesting to note that many false-positive classifications of pulses resulting from the previous algorithm [14,15] are removed due to the change in the PGV threshold.

Specifically, this happens for the L'Aquila (AQV and AQG stations), Accumoli (AMT, NRC and FEMA stations) and Ussita (NOR station) near-fault ground motions (Table 2a). Moreover, the potential pulses of the near-fault EQs worldwide exhibit PI values (Table 2b) markedly higher than those obtained for the central Italy EQs (Table 2a). Finally, the direction of the dominant pulse, chosen as the pulse with highest wavelet coefficient, does not correspond to the fault-normal orientation for all Italian (see L'Aquila, AQA and AQK stations in Fig. 1a, and Accumoli, NOR station in Fig. 1b, EQs) and one worldwide (see Taiwan EQ, TCU068 station in Fig. 2a).

Finally, the elastic response spectra of acceleration for the original ground motion, extracted pulse and residual ground motion of the Italian and worldwide EQs are shown in Fig. 3, by vertical dashed line highlighting the $T_P$ value determined through wavelet analysis. Specifically, only the direction of the dominant pulse (i.e. the potential pulse n.1 in Tables 2a and 2b) is considered for each ground motion, assuming an equivalent viscous damping ($\xi$) equal to 5%. The corresponding NTC08 response spectra at the collapse prevention limit state [33], assuming high-risk seismic region and two subsoil classes (i.e. ground types C and D of the Italian seismic code), are also reported for reference. In terms of spectral values, the extracted pulse is a minor feature of the ground motion and the residual motion is nearly identical with the original one for vibration periods rather less than the $T_P$ value. Moreover, it is apparent that the extracted pulses cause amplification of the spectra in the region of the vibration periods higher than the $T_P$ value, even if the pulse period is not a strict dividing line between regions in which residual motion and extracted pulse are dominant. As a confirmation, Fourier spectra of the original ground motion, extracted pulse and residual ground motion are shown in Fig. 4 for the Italian and worldwide EQs.

However, spectral values of the selected earthquakes are quite different from those corresponding to the NTC08 spectra, in the range of long vibration periods (i.e. T > 2.5 s) which are more significant for the base-isolated test structures, so requiring evaluation of suitable scale factors. The selection of an intensity measure to predict structural demand of base-isolated buildings subjected to near-fault ground motions is a difficult task, because ground motions characterized by similar spectral values at specific vibration periods can produce different structural responses due to lengthening of the vibration period as the structure goes well into the inelastic range.

In the present work, the *Modified Velocity Spectrum Intensity* (*MVSI*), obtained from integration of the velocity (elastic) response spectra of the horizontal components (i.e. H1 and H2) of the near-fault earthquakes over a defined range of vibration periods (i.e. $0.5T_1$-$1.25T_1$, being $T_1$ the fundamental vibration period of the base-isolated structure), is adopted [39]

$$MVSI_{\text{near-fault,H1}} = \int_{0.5T_1}^{1.25T_1} S_{v,H1}(T, \xi)\cdot dT,\ MVSI_{\text{near-fault},H2} = \int_{0.5T_1}^{1.25T_1} S_{v,H2}(T, \xi)\cdot dT \tag{6}$$

Then, a mean value of the intensity measure is obtained by combining the MVSI values

$$MVSI_{\text{near-fault}} = \frac{MVSI_{\text{near-fault,H1}} + MVSI_{\text{near-fault,H2}}}{2} \tag{7}$$

Finally, the selected real accelerograms are normalized with respect to the NTC08 ones by scaling their *PGA* values

$$PGA_S = PGA/SF_{MVSI} \tag{8}$$

through the scale factor

**Table 1b**
Near-fault earthquakes worldwide (PEER-NGA database [35]).

| *Earthquake (EQ)* | *Recording station* | $\Delta_2$ (km) | $PGA_{H1}$ (m/s$^2$) | $PGA_{H2}$ (m/s$^2$) | $PGA_V$ (m/s$^2$) | $PGV_{H,max}$ (cm/s) | $PGD_{H,max}$ (cm) |
|---|---|---|---|---|---|---|---|
| Chi-Chi (Taiwan), 20/9/1999 ($M_w$ = 7.6) | TCU068 | 0.32 | 5.02 | 3.64 | 5.20 | 263.97 | 421.46 |
| Northridge (California), 17/1/1994 ($M_w$ = 6.7) | Rinaldi | 6.50 | 8.57 | 4.63 | 9.40 | 147.92 | 41.85 |
| Kobe (Japan), 16/1/1995 ($M_w$ = 6.9) | Takatori | 1.47 | 6.06 | 6.58 | 2.79 | 122.90 | 39.92 |

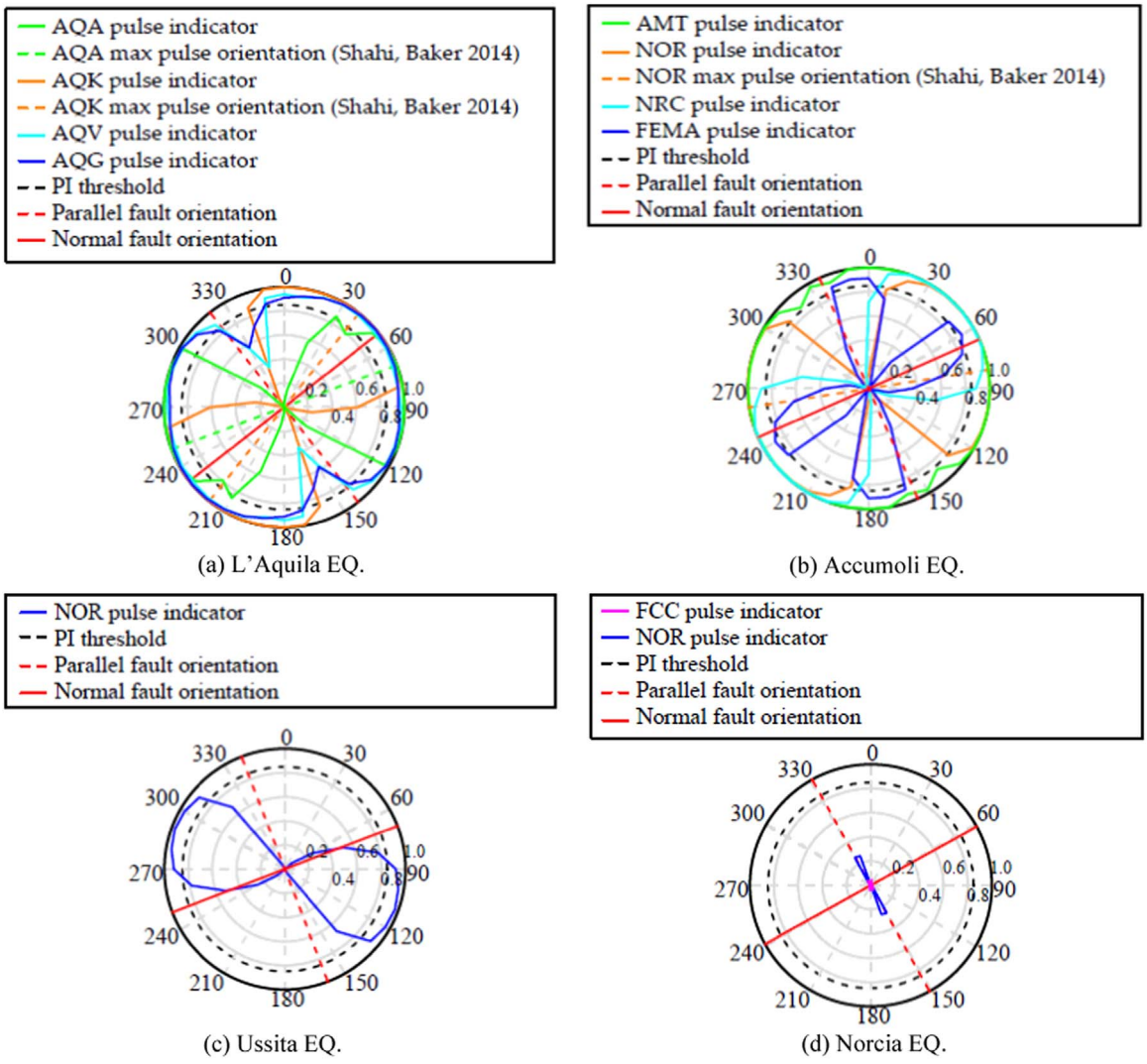


**Fig. 1.** Pulse Indicator values [14,15] of near-fault earthquakes in central Italy as function of the orientation.

$$SF_{MVSI} = MVSI_{\text{near-fault}}/MVSI_{NTC08} \quad (9)$$

Note that different values of the scale factor are obtained for the EBI and SBI structures, because each of them is characterized by a fundamental vibration period selected in order to satisfy the collapse prevention limit state verifications. Further details can be found in the following section.

As a comparison, the scale factors used to normalize the Italian and worldwide near-fault earthquakes are reported in Tables 3a and 3b, respectively, for base-isolated structures with elastomeric (EBI) and sliding (SBI) bearings and subsoil classes C and D [33]. As expected, the SFs for the central Italy earthquakes (Table 3a) are higher than those obtained for the worldwide EQs (Table 3b) while, for the same earthquake, there is an increase of the scale factor increasing the subsoil deformability (i.e. considering subsoil D instead of C). Finally, the main corresponding potential pulse for each normalized records are reported in Tables 4a and 4b.

## 3. Layout and simulated design of the in-plan irregular fixed-base structure

A five-storey L-shaped residential building (Fig. 5a) with reinforced concrete (r.c.) framed structure (Fig. 5b, c), chosen from case-studies of the Re.L.U.I.S. project as representative of a spread typology in Italy, is considered for the numerical investigation [40]. In-plan irregularity due to bays of different length is also assumed along both principal directions. The floors are of one-way ribbed concrete slabs supported by deep beams (thick lines, Fig. 5a) while flat beams are placed parallel to the slab direction to complete the floor structure (thin lines, Fig. 5a). A simulated design of the original framed building is carried out in accordance with the previous Italian code (DM96, [41]), for medium-risk seismic region (seismic coefficient, C = 0.07; response coefficient, R = 1; structure coefficient, β = 1) and typical subsoil class (foundation coefficient, $\varepsilon$ = 1). A cylindrical compressive strength of 25 N/mm$^2$ for the concrete and a yield strength of 375 N/mm$^2$ for the steel are considered. The gravity loads used in the design are represented by: a dead load of 5.82 kN/m$^2$, for the top floor, and 7.12 kN/m$^2$, for the other ones; a live load of 2 kN/m$^2$ for all the floors; an additional snow load of 0.48 kN/m$^2$ for the roof, which is only considered for the combination of vertical loads. A masonry-infill is regularly distributed in elevation along the perimeter, assuming an average weight of 1.89 kN/m$^2$. The design of the test structure complies with the ultimate limit states. Details for local ductility are also imposed to satisfy minimum conditions for the longitudinal bars of the r.c. frame members [41].

Dynamic properties of the five main vibration modes are reported in Table 5a: i.e. vibration period (T); translational effective masses in the X ($m_{E,X}$) and Y ($m_{E,Y}$) directions and rotational effective mass around the Z direction ($m_{E,rZ}$), expressed as a percentage of the total mass ($m_{tot}$). The dimensions of the cross sections assumed for the beams, constant along the height of the building with the only exception being

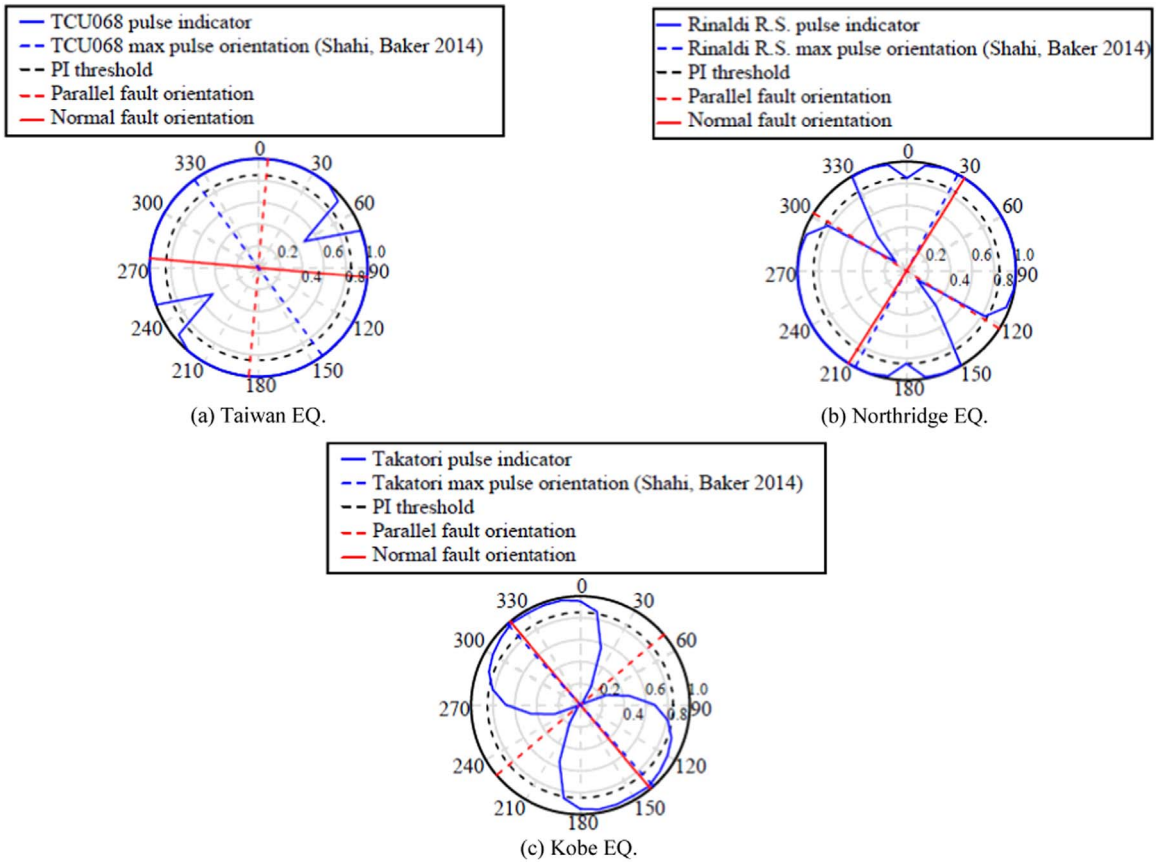


**Fig. 2.** Pulse Indicator values [14,15] of near-fault earthquakes worldwide as function of the orientation.

**Table 2a**
Potential pulses of near-fault earthquakes in central Italy [16].

| *Earthquake (EQ)* | *Recording station* | *Potential pulse n.1* | | | *Potential pulse n.2* | | |
|---|---|---|---|---|---|---|---|
| | | *α (°)* | *$T_p$[s]* | *PI* | *α (°)* | *$T_p$[s]* | *PI* |
| L'Aquila | AQV | – | – | – | – | – | – |
| | AQG | – | – | – | – | – | – |
| | AQA | 70 | 1.18 | 0.13 | – | – | – |
| | AQK | 38 | 1.98 | 3.98 | 39 | 2.10 | 3.94 |
| Accumoli (Rieti) | AMT | – | – | – | – | – | – |
| | NRC | – | – | – | – | – | – |
| | NOR | 81 | 1.65 | 0.55 | – | – | – |
| | FEMA | – | – | – | – | – | – |
| Ussita (Rieti) | NOR | – | – | – | – | – | – |
| Norcia (Rieti) | FCC | – | – | – | – | – | – |
| | NOR | – | – | – | – | – | – |

beam 5–6 (Fig. 5a), and columns, regularly tapering in elevation, are reported in Table 5c. Moreover, the centre of mass (CM) is shown in Fig. 5 and eccentricities (i.e. $e_X$ and $e_Y$) at the floor levels are presented in Table 5b, expressed as distance of the centre of lateral stiffness (CS) from CM. A torsionally stiff structure is found considering the X and Y directions at each level, the ratio between the torsional radius (i.e. $r_X$ and $r_Y$) and the radius of gyration of the floor mass (i.e. $l_s$) being greater than the limit value 0.8 prescribed by NTC08 (see Table 5b).

## 4. Retrofitted base-isolated structures

The use of the base-isolation system is focused on the seismic retrofitting of the residential building above described, in L'Aquila and Accumoli (Rieti) where similar spectral values of acceleration for the geographical coordinates at the selected sites are obtained. Base-isolation with elastomeric (EBI) and sliding (SBI) bearings is considered to retrofit the original fixed-base (FB) framed building, for attaining performance levels imposed by current Italian code (NTC08, [33]) in a high-risk seismic zone (peak ground acceleration on rock, $a_g$ = 0.334 g at the collapse prevention limit state) and for moderately-soft and soft subsoils (i.e. class C, site amplification factor S = 1.219; class D, site amplification factor S = 1.198). Specifically, eight structural solutions are examined for the base-isolation system, identifying each retrofitted base-isolated structure by two characters following the acronym EBI or SBI: the first corresponds to the seismic loads (i.e. H or HV when considering the horizontal component of the seismic loads acting alone or in combination with the vertical one, respectively); the second refers to

**Table 2b**
Potential pulses of near-fault earthquakes worldwide [16].

| *Earthquake (EQ)* | *Potential pulse n.1* | | | *Potential pulse n.2* | | | *Potential pulse n.3* | | | *Potential pulse n.4* | | |
|---|---|---|---|---|---|---|---|---|---|---|---|---|
| | α (°) | $T_p$ [s] | *PI* | α (°) | $T_p$ [s] | *PI* | α (°) | $T_p$ [s] | *PI* | α (°) | $T_p$ [s] | *PI* |
| Chi-Chi (Taiwan) | 144 | 12.3 | 65.2 | 148 | 10.47 | 65.9 | 142 | 14.36 | 56.8 | 130 | 15.29 | 42 |
| Northridge (California) | 209 | 1.25 | 27.3 | 211 | 1.48 | 25.2 | – | – | – | – | – | – |
| Kobe (Japan) | 318 | 1.55 | 8.7 | 324 | 1.85 | 4.2 | 338 | 2.38 | 7.4 | – | – | – |

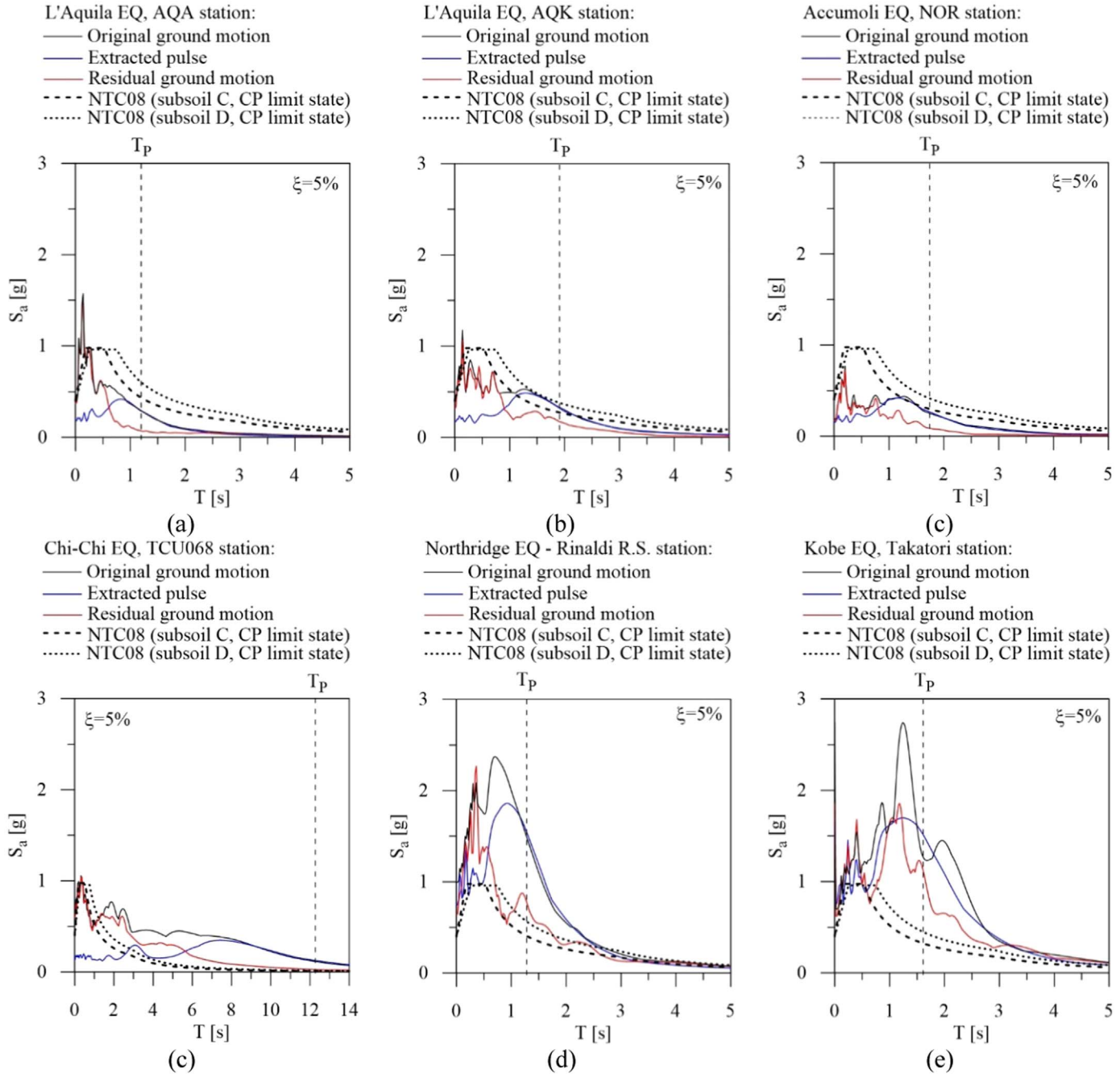


**Fig. 3.** Spectral acceleration for near-fault earthquakes in central Italy and worldwide.

the subsoil class (i.e. C or D).

### 4.1. Elastomeric bearings: design and nonlinear modelling

The design of the elastomeric (i.e. high-damping-laminated-rubber bearings, HDLRBs) base-isolation system is carried out on the assumption that the same values of the equivalent viscous damping ratio are considered for the four EBI structures: i.e. $\xi_H = 15\%$, in the horizontal direction; $\xi_V = 5\%$ in the vertical direction. Moreover, the fundamental vibration periods of the base-isolated structures satisfy the condition $T_{I,X} \equiv T_{I,Y} \geq \max(3T_{BF,X}, 3T_{BF,Y})$, $T_{BF,X}$ and $T_{BF,Y}$ being the fundamental vibration periods of the same structure on fixed-base (see Table 5a). In particular, dynamic properties of the EBI structures are reported in Table 6a, confiming that torsional coupling is magnified for asymmetric plan layouts when elastomeric bearings are adopted [22,31,32]. A nominal stiffness ratio $\alpha_{K0}$, defined as the ratio between the nominal value of the vertical stiffness ($K_{V0}$) and the analogous value of the horizontal stiffness ($K_{H0}$), equal to 1400 is assumed for all the isolators, considering a volumetric compression modulus of the rubber (i.e. $E_b$) equal to 2000 MPa and a shear modulus G = 0.35 MPa. An additional mass of 465 ton is assumed at the level of the beams, with a cross section of 50 × 100 $cm^2$, placed above the isolators.

Two in-plan configurations of HDLRBs include: i) nineteen isolators with same dimensions (i.e. HDLRBs type 1 shown in Fig. 6a), that in comparison with dimensions proportional to the vertical load acting on each isolator allows an increase of the torsional stiffness of the base-isolation system increasing the later stiffness of perimeter and corners isolators; ii) nine HDLRBs type 1 combined with ten HDLRBs type 2 (Fig. 6b), to avoid excessive compressive and tensile loads in the isolators when subsoil class D is considered.

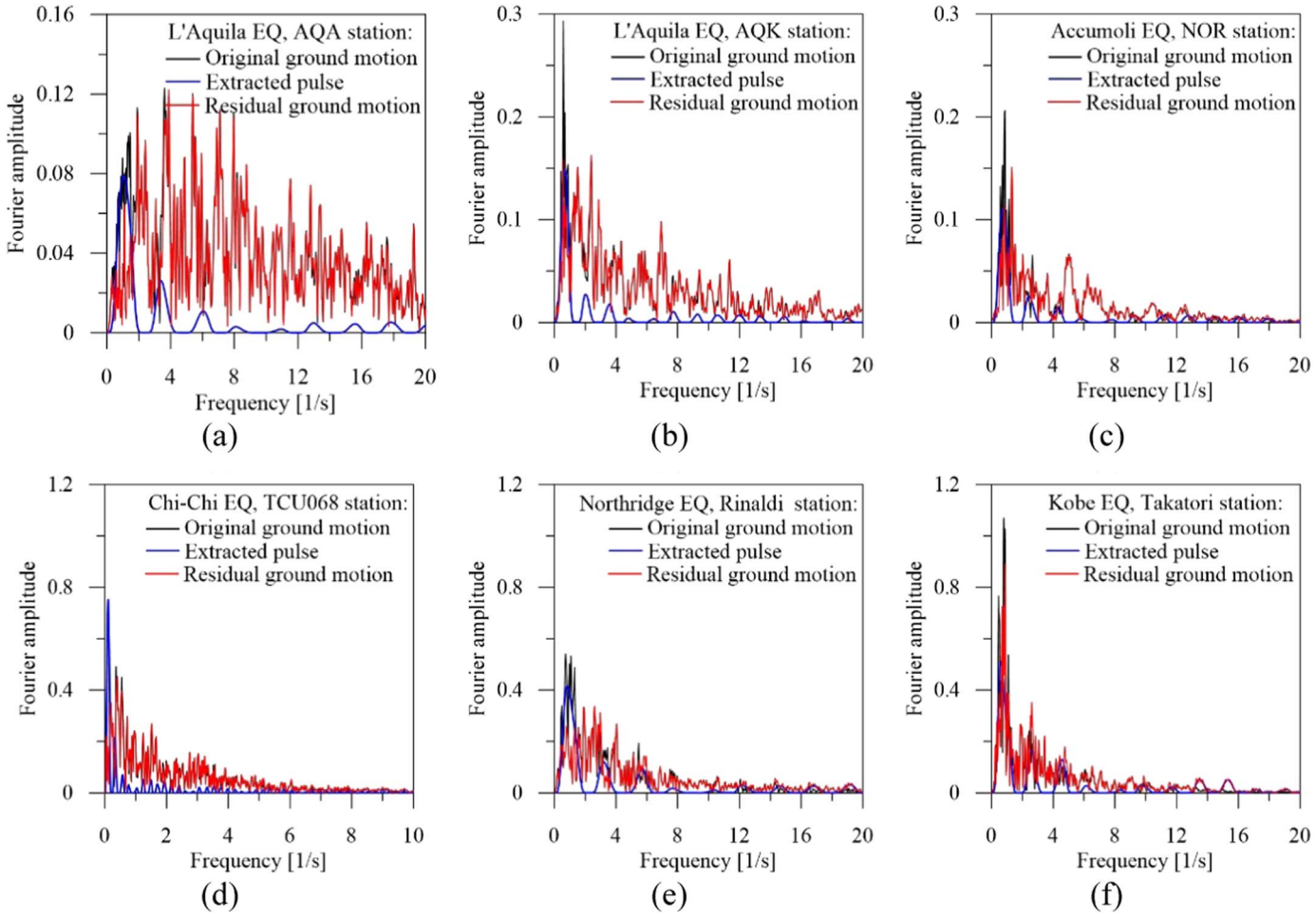


**Fig. 4.** Fourier spectra for near-fault earthquakes in central Italy and worldwide.

**Table 3a**
Scale factors of near-fault earthquakes in central Italy assuming the MVSI measure.

| *Earthquake (EQ)* | *Recording station* | *Scale factor (subsoil C)* | | *Scale factor (subsoil D)* | |
|---|---|---|---|---|---|
| | | *EBI* | *SBI* | *EBI* | *SBI* |
| L'Aquila, 6/4/2009 ($M_w$ = 6.3) | AQV | 1.56 | 1.61 | 2.22 | 2.22 |
| | AQG | 1.63 | 1.64 | 2.29 | 2.24 |
| | AQA | 2.18 | 2.25 | 3.10 | 3.09 |
| | AQK | 1.19 | 1.29 | 1.74 | 1.91 |
| Accumoli (Rieti), 24/8/2016 ($M_w$ = 6.0) | AMT | 3.21 | 3.24 | 4.50 | 4.37 |
| | NRC | 1.92 | 1.99 | 2.73 | 2.80 |
| | NOR | 1.58 | 1.71 | 2.31 | 2.44 |
| | FEMA | 4.67 | 4.70 | 6.56 | 6.31 |
| Ussita (Rieti), 26/10/2016 ($M_w$ = 5.9) | NOR | 3.61 | 3.62 | 5.06 | 4.99 |
| Norcia (Rieti), 30/10/2016 ($M_w$ = 6.5) | FCC | 0.93 | 0.94 | 1.30 | 1.29 |
| | NOR | 0.79 | 0.88 | 1.18 | 1.27 |

**Table 3b**
Scale factors of near-fault earthquakes worldwide assuming the MVSI measure.

| *Earthquake (EQ)* | *Recording station* | *Scale factor (subsoil C)* | | *Scale factor (subsoil D)* | |
|---|---|---|---|---|---|
| | | *EBI* | *SBI* | *EBI* | *SBI* |
| Chi-Chi (Taiwan), 20/9/1999 ($M_w$ = 7.6) | TCU068 | 0.45 | 0.42 | 0.60 | 0.52 |
| Northridge (California), 17/1/1994 ($M_w$ = 6.7) | Rinaldi Rec. Sta. | 0.44 | 0.45 | 0.62 | 0.62 |
| Kobe (Japan), 16/1/1995 ($M_w$ = 6.9) | Takatori | 0.32 | 0.34 | 0.48 | 0.50 |

In detail, the HDLRBs fulfill the collapse prevention (ultimate) limit state verifications regarding the maximum shear strains: i.e. $\gamma_{tot} \leq 5$ and $\gamma_s \leq 2$, where $\gamma_{tot}$ represents the total design shear strain and $\gamma_s$ represent the shear strain of the elastomer due to seismic displacement. Moreover, the maximum compression axial load (P) does not exceed the critical load divided by a safety coefficient equal to 2.0, while the minimum tensile stress ($\sigma_t$) resulting from the seismic analysis is assumed as 2G (=0.7 MPa). In Table 6b the mechanical properties of the base isolation system are reported: i.e. the horizontal ($K_{H0}$) and vertical ($K_{V0}$) nominal stiffnesses and the corresponding equivalent damping coefficients ($C_H$ and $C_V$). Moreover, the following geometric properties of the HDLRBs are reported in Table 6c: i.e. eccentricities ($e_X$ and $e_Y$) between mass and stiffness centres of the superstructure and base-isolation system, respectively; diameter of the bearings ($D$); primary ($S_1$) and secondary ($S_2$) shape factors; displacement at the collapse prevention limit state ($d_{dC}$).

Finally, the results of the verifications for the HDLRBs are reported in Table 6d. Note that the design of the isolators largely depends on the condition imposed on the minimum tensile stress ($\sigma_t$) and maximum compression axial load (P), whose limit values are reached for the isolators shown in Fig. 6a, b.

Experimental results indicate coupling of the horizontal and vertical

**Table 4a**
Potential pulses of scaled near-fault earthquakes in central Italy [16].

| *Earthquake (EQ)* | *Recording station* | *Potential pulse n.1* | | | |
|---|---|---|---|---|---|
| | | *α (°)* | *$T_p$ [s]* | *PI (subsoil class C)* | *PI (subsoil class D)* |
| L'Aquila | AQV | 110 | 1.06 | 2.73 | 5.10 |
| | AQG | 63 | 0.99 | 1.98 | 4.35 |
| | AQA | 70 | 1.18 | 7.25 | 11.31 |
| | AQK | 38 | 1.98 | 6.76 | 12.21 |
| Accumoli (Rieti) | AMT | 10 | 0.90 | 10.11 | 15.07 |
| | NRC | 49 | 2.07 | 5.69 | 10.10 |
| | NOR | 81 | 1.65 | 5.59 | 10.44 |
| | FEMA | / | / | / | / |
| Ussita (Rieti) | NOR | 108 | 1.18 | 3.52 | 6.01 |
| Norcia (Rieti) | FCC | / | / | / | / |
| | NOR | / | / | / | / |

**Table 4b**
Potential pulses of scaled near-fault earthquakes worldwide [16].

| *Earthquake (EQ)* | *Potential pulse n.1* | | | |
|---|---|---|---|---|
| | *α (°)* | *$T_p$ [s]* | *PI (subsoil class C)* | *PI (subsoil class D)* |
| Chi-Chi (Taiwan) | 144 | 12.29 | 34.88 | 42.50 |
| Northridge (California) | 209 | 1.25 | 10.68 | 16.41 |
| Kobe (Japan) | 318 | 1.55 | 1.16 | 3.79 |

**Table 5a**
Dynamic properties ($m_{tot}$ = 1626 ton).

| *Mode* | *T (s)* | *$m_{e,X}$ (%$m_{tot}$)* | *$m_{e,Y}$ (%$m_{tot}$)* | *$m_{e,rZ}$ (%$m_{tot}$)* |
|---|---|---|---|---|
| 1 | 0.918 | 9.60 | 45.70 | 5.53 |
| 2 | 0.764 | 50.20 | 24.71 | 0.052 |
| 3 | 0.633 | 20.22 | 10.03 | 74.82 |
| 4 | 0.312 | 0.98 | 7.91 | 0.92 |
| 5 | 0.262 | 8.68 | 2.88 | 0.00 |

**Table 5b**
Eccentricities between mass and stiffness centres (units in cm).

| *Floor level* | *$e_X$* | *$e_Y$* | *$r_X/l_s$* | *$r_Y/l_s$* |
|---|---|---|---|---|
| 1 | 218.1 | 119.5 | 1.11 | 1.25 |
| 2 | 255.0 | 175.4 | 1.10 | 1.22 |
| 3 | 259.1 | 187.6 | 1.09 | 1.21 |
| 4 | 250.2 | 190.1 | 1.10 | 1.21 |
| 5 | 253.1 | 194.6 | 1.11 | 1.24 |

responses of HDLRBs [42], with horizontal (starting from $K_{H0}$) and vertical (starting from $K_{V0}$) stiffnesses decreasing with increase of vertical load (P) and lateral deformation ($u_H$), respectively. To account for the observed behaviour, a three-spring-three-dashpot generalization of a previous model [9], constituted of a nonlinear spring acting in parallel with a linear viscous dashpot both in the two horizontal directions and in the vertical one, can be adopted. The nonlinear restoring force for the

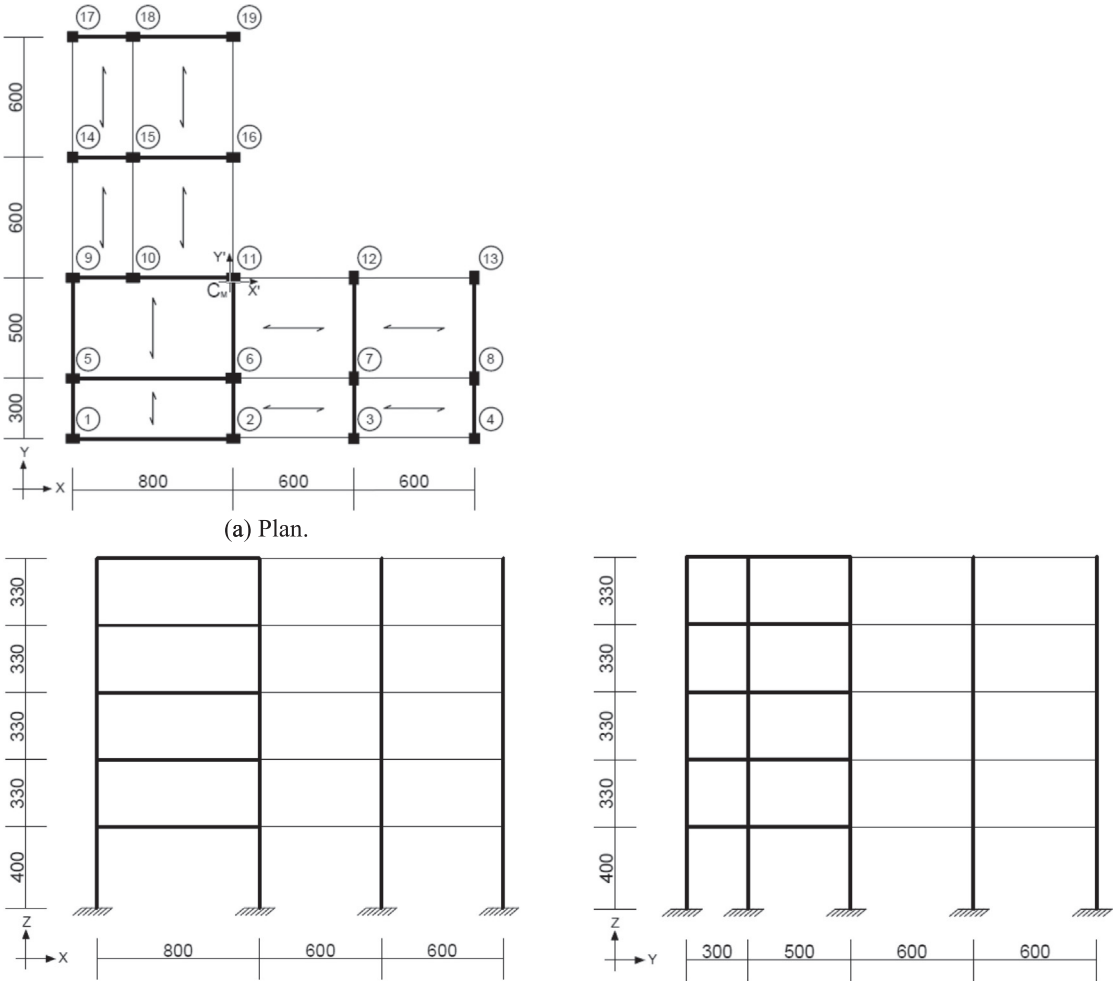


**Fig. 5.** Fixed-base (original) test structure (units in m).

**Table 5c**
Cross-section dimensions of beams and columns (units in cm).

| *Joint i* | *Joint j* | *Beam* | *Column* | *Storey n.1* | *Storey n.2* | *Storey n.3* | *Storey n.4* | *Storey n.5* |
|---|---|---|---|---|---|---|---|---|
| 1 | 2 | 30 × 50 | 1 | 65 × 45 | 60 × 40 | 55 × 35 | 50 × 35 | 45 × 30 |
| 2 | 4 | 50 × 25 | 2 | 65 × 45 | 60 × 40 | 55 × 35 | 50 × 35 | 45 × 30 |
| 5 | 6 | 40 × 70* | 3 | 50 × 50 | 45 × 45 | 35 × 35 | 30 × 30 | 30 × 30 |
| 5 | 6 | 30 × 70 | 4 | 50 × 50 | 45 × 45 | 35 × 35 | 30 × 30 | 30 × 30 |
| 6 | 8 | 50 × 25 | 5 | 65 × 45 | 60 × 40 | 55 × 35 | 50 × 35 | 45 × 30 |
| 9 | 11 | 30 × 70 | 6 | 70 × 50 | 70 × 45 | 65 × 45 | 60 × 40 | 50 × 40 |
| 11 | 13 | 50 × 25 | 7 | 45 × 65 | 40 × 60 | 35 × 55 | 35 × 50 | 30 × 45 |
| 14 | 16 | 30 × 70 | 8 | 45 × 65 | 40 × 60 | 35 × 55 | 35 × 50 | 30 × 45 |
| 17 | 19 | 50 × 50 | 9 | 65 × 45 | 60 × 40 | 55 × 35 | 50 × 35 | 45 × 30 |
| 1 | 9 | 30 × 50 | 10 | 65 × 45 | 60 × 40 | 55 × 35 | 50 × 35 | 45 × 30 |
| 2 | 11 | 30 × 60 | 11 | 65 × 45 | 60 × 40 | 55 × 35 | 50 × 35 | 45 × 30 |
| 3 | 12 | 30 × 70 | 12 | 45 × 65 | 40 × 60 | 35 × 55 | 35 × 50 | 30 × 35 |
| 4 | 13 | 30 × 50 | 13 | 45 × 65 | 40 × 60 | 35 × 55 | 35 × 50 | 30 × 45 |
| 9 | 17 | 50 × 25 | 14 | 50 × 50 | 45 × 45 | 35 × 35 | 30 × 30 | 30 × 30 |
| 10 | 18 | 50 × 25 | 15 | 65 × 45 | 60 × 40 | 55 × 35 | 50 × 35 | 45 × 30 |
| 11 | 19 | 50 × 25 | 16 | 65 × 45 | 60 × 40 | 55 × 35 | 50 × 35 | 45 × 30 |
| *First and second floor. | | | 17 | 50 × 50 | 45 × 45 | 35 × 35 | 30 × 30 | 30 × 30 |
| | | | 18 | 65 × 45 | 60 × 40 | 55 × 35 | 50 × 35 | 45 × 30 |
| | | | 19 | 65 × 45 | 60 × 40 | 55 × 35 | 50 × 35 | 45 × 30 |

**Table 6a**
Dynamic properties of the EBI structures ($m_{tot}$ = 2091 ton).

| *Structure* | *Mode* | *Vibration period* (s) | $m_{e,X}$ (%$m_{tot}$) | $m_{e,Y}$ (%$m_{tot}$) | $m_{e,rZ}$ (%$m_{tot}$) |
|---|---|---|---|---|---|
| | 1 | 2.602 | 25.97 | 69.44 | 36.90 |
| EBI.HC | 2 | 2.580 | 70.07 | 28.79 | 1.05 |
| | 3 | 2.338 | 0.04 | 0.02 | 61.93 |
| | 1 | 2.710 | 27.05 | 68.59 | 37.60 |
| EBI.HVC | 2 | 2.689 | 69.16 | 29.78 | 0.93 |
| | 3 | 2.437 | 0.04 | 0.01 | 61.38 |
| | 1 | 2.934 | 16.48 | 80.97 | 38.51 |
| EBI.HD | 2 | 2.916 | 81.49 | 17.74 | 4.53 |
| | 3 | 2.661 | 0.02 | 0.01 | 56.88 |
| | 1 | 2.916 | 81.49 | 17.74 | 37.55 |
| EBI.HVD | 2 | 2.986 | 11.03 | 87.08 | 8.06 |
| | 3 | 2.719 | 0.01 | 0.01 | 54.32 |

horizontal ($F_K$) and vertical ($P_K$) directions are:

$$F = K_{H0}[1 - (P/P'_{cr})^2] \begin{Bmatrix} u_{H,x} \\ u_{H,y} \end{Bmatrix} + C_H \begin{Bmatrix} \dot{u}_{H,x} \\ \dot{u}_{H,y} \end{Bmatrix} \quad (10)$$

**Table 6b**
Mechanical properties of the HDLRBs (units in kN, s and cm).

| | *HDLRB type 1* | | | | *HDLRB type 2* | | | |
|---|---|---|---|---|---|---|---|---|
| *Structure* | $K_{H0}$ | $K_{V0}$ | $C_H$ | $C_V$ | $K_{H0}$ | $K_{V0}$ | $C_H$ | $C_V$ |
| EBI.HC | 6.92 | 9672 | 0.83 | 10.32 | / | / | / | / |
| EBI.HVC | 6.34 | 8870 | 0.79 | 9.86 | / | / | / | / |
| EBI.HD | 5.13 | 7080 | 0.73 | 9.08 | 5.50 | 7670 | 0.73 | 9.13 |
| EBI.HVD | 4.82 | 6750 | 0.71 | 8.88 | 5.38 | 7530 | 0.72 | 8.95 |

$$P = \frac{K_{V0}}{1 + 48\frac{u_{H,x}^2 + u_{H,y}^2}{\pi^2 D^2}} \left[ u_V - \frac{\alpha_b}{\alpha_{K0}} \frac{16}{\pi^2 D S_2} (u_{H,x}^2 + u_{H,y}^2) \right] + C_V \dot{u}_V \quad (11)$$

where $\alpha_b = h_b/t_r$, $h_b$ being the total height of the bearing and $t_r$ the total thickness of the rubber, and $P'_{cr}$ is the critical buckling load decreasing with increase in the horizontal displacement as function of the reduced effective area ($A_r$) defined as the area of overlap between the top and bottom of the isolator [43].

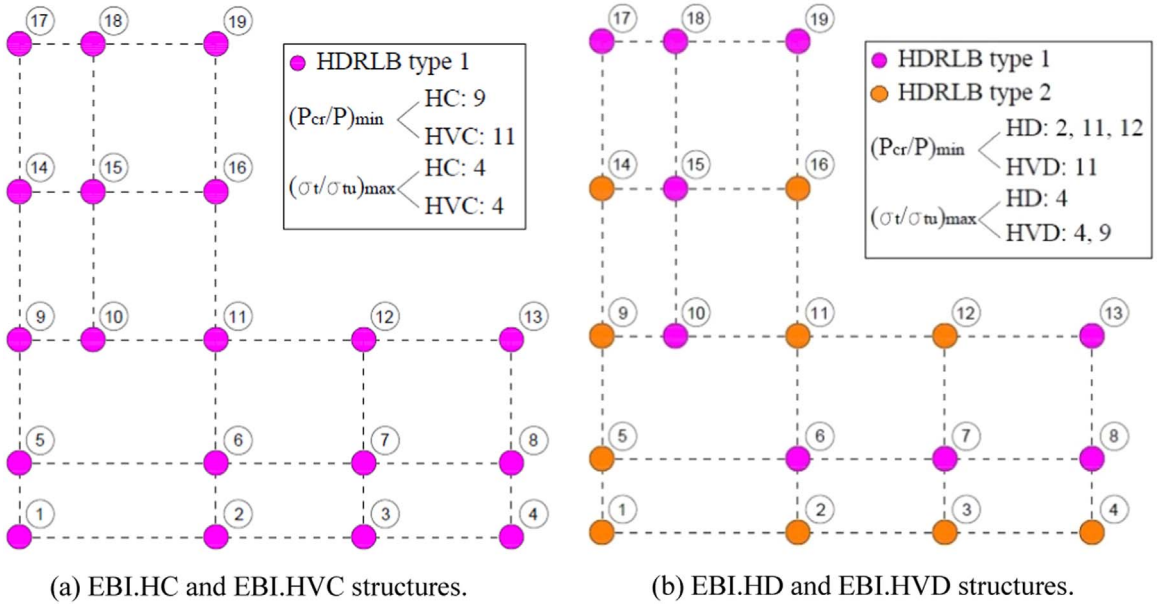


(a) EBI.HC and EBI.HVC structures. (b) EBI.HD and EBI.HVD structures.

**Fig. 6.** Base-isolated (retrofitted) test structures: in-plan distributions of HDLRBs.

**Table 6c**
Geometric properties of the HDLRBs (units in cm).

| *Structure* | $e_X$ | $e_Y$ | $D_{type\ 1}$ | $D_{type\ 2}$ | $S_{1,type\ 1}$ | $S_{2,type\ 1}$ | $S_{1,type\ 2}$ | $S_{2,type\ 2}$ | $d_{dC}$ |
|---|---|---|---|---|---|---|---|---|---|
| EBI.HC | 35.5 | 19.7 | 74 | / | 18.60 | 3.38 | / | / | 27 |
| EBI.HVC | 35.5 | 19.7 | 74 | / | 18.60 | 3.10 | / | / | 28 |
| EBI.HD | 26.0 | 17.0 | 89 | 95 | 18.44 | 18.56 | 2.11 | 2.12 | 42 |
| EBI.HVD | 17.7 | 15.5 | 90 | 100 | 18.63 | 18.62 | 1.96 | 1.96 | 42 |

**Table 6d**
Results of the verifications for the HDLRBs.

| | *HDLRB type 1* | | | | *HDLRB type 2* | | | |
|---|---|---|---|---|---|---|---|---|
| *Structure* | $\gamma_{s,max}$ | $\gamma_{tot,max}$ | $(P_{cr}/P)_{min}$ | $(\sigma_t/\sigma_{tu})_{max}$ | $\gamma_{s,max}$ | $\gamma_{tot,max}$ | $(P_{cr}/P)_{min}$ | $(\sigma_t/\sigma_{tu})_{max}$ |
| EBI.HC | 1.22 | 3.11 | 2.58 | 0.73 | / | / | / | / |
| EBI.HVC | 1.17 | 3.23 | 2.11 | 0.91 | / | / | / | / |
| EBI.HD | 0.99 | 2.40 | 2.26 | 0.74 | 0.98 | 2.48 | 2.01 | 0.99 |
| EBI.HVD | 0.93 | 2.34 | 2.10 | 0.92 | 0.98 | 2.19 | 2.03 | 0.98 |

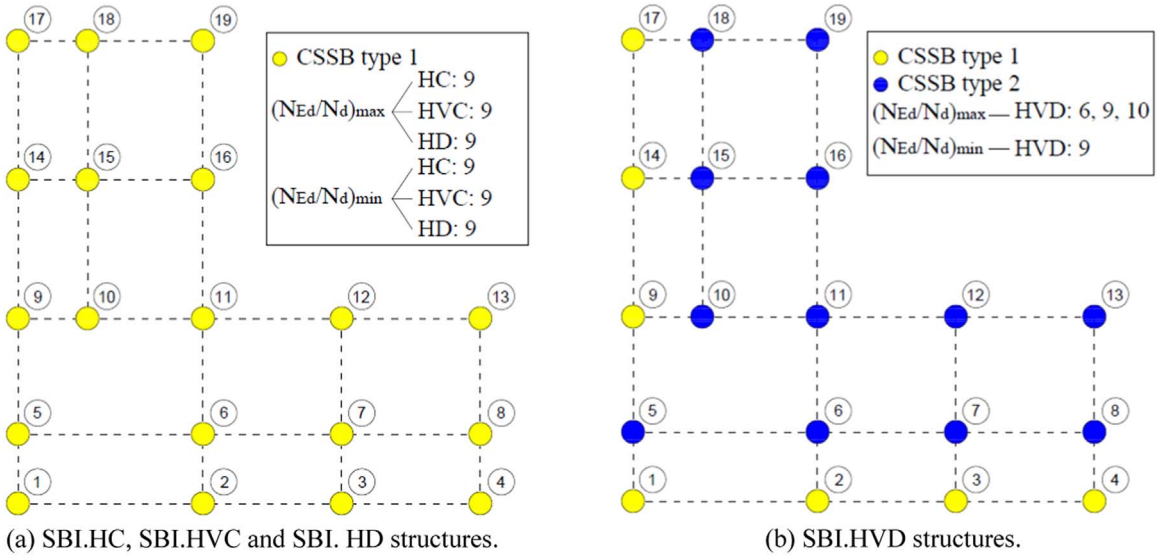


(a) SBI.HC, SBI.HVC and SBI. HD structures. (b) SBI.HVD structures.

**Fig. 7.** Base-isolated (retrofitted) test structures: in-plan distributions of CSSBs.

**Table 7a**
Dynamic properties of the SBI structures ($m_{tot}$ = 2091 ton).

| *Structure* | *Mode* | *Vibration period* (s) | $m_{e,X}$ (%$m_{tot}$) | $m_{e,Y}$ (%$m_{tot}$) | $m_{e,rZ}$ (%$m_{tot}$) |
|---|---|---|---|---|---|
| SBI.HC | 1 | 3.098 | 10.25 | 42.79 | 1.10 |
| | 2 | 3.073 | 41.63 | 46.20 | 5.67 |
| | 3 | 3.061 | 48.05 | 10.92 | 93.19 |
| SBI.HVC | 1 | 3.250 | 9.96 | 41.12 | 0.75 |
| | 2 | 3.226 | 39.74 | 47.91 | 6.49 |
| | 3 | 3.216 | 50.25 | 10.89 | 92.73 |
| SBI.HD | 1 | 3.599 | 9.42 | 36.49 | 0.15 |
| | 2 | 3.576 | 31.72 | 54.45 | 10.88 |
| | 3 | 3.568 | 58.83 | 9.01 | 88.95 |
| SBI.HVD | 1 | 3.858 | 0.34 | 47.28 | 74.86 |
| | 2 | 3.840 | 43.62 | 26.72 | 9.29 |
| | 3 | 3.836 | 56.02 | 25.96 | 15.83 |

### 4.2. Sliding bearings: design and nonlinear modelling

The design of the sliding (i.e. curved surface sliding bearings, CSSBs) base-isolation system for the EBI structures is carried out on the assumption that the same radius of curvature (R) is considered for all the isolators, while constant or variable dynamic-fast friction coefficients ($\mu_{fast}$) are assumed in order to obtain maximum compression

**Table 7b**
Geometric and mechanical properties of the CSSBs (units in cm).

| *Structure* | *Viscous damping* [%] | $e_X$ | $e_Y$ | $R$ | $d_{dC}$ |
|---|---|---|---|---|---|
| SBI.HC | 31.60 | 0.069 | 0.063 | 450 | 25 |
| SBI.HVC | 34.65 | 0.057 | 0.068 | 550 | 25 |
| SBI.HD | 30.79 | 0.060 | 0.063 | 600 | 35 |
| SBI.HVD | 31.00 | 0.020 | 0.039 | 700 | 35 |

axial load of the CSS bearings lower than their capacity ($N_{Ed}$) and absence of tensile axial load at the level of the CSS system. Specifically, an iterative procedure is used to evaluate design parameters of the CSSs on the basis of the expressions of the effective fundamental vibration period of the isolation system and effective equivalent viscous damping depending on spectral displacement at the collapse prevention limit state ($d_{dC}$). Then, an experimental law for low-type friction properties [44], taking into account the variability of the dynamic-fast friction coefficient with the axial load

$$\mu_{fast}(\%) = 2.5\left(\frac{N_{Sd}}{N_{Ed}}\right)^{-0.834}, \quad \left(\frac{N_{Sd}}{N_{Ed}}\right) > 0.1 \tag{12}$$

is adopted to evaluate the maximum axial load capacity of the CSSBs

**Table 7c**
Local design parameters of the CSS bearings (units in kN).

| | | $\mu_{fast}$ (%) | | | | $N_{Ed}$ | | | |
|---|---|---|---|---|---|---|---|---|---|
| $CSSB_i$ | $N_{Sd}$ | SBI.HC | SBI.HVC | SBI.HD | SBI.HVD | SBI.HC | SBI.HVC | SBI.HD | SBI.HVD |
| 1 | 729 | 4.5 | 4.5 | 4.5 | 4.4 | 1488 | 1474 | 1473 | 1450 |
| 2 | 1091 | 4.5 | 4.5 | 4.5 | 4.1 | 2227 | 2207 | 2206 | 2000 |
| 3 | 845 | 4.5 | 4.5 | 4.5 | 4.1 | 1725 | 1709 | 1710 | 1550 |
| 4 | 508 | 4.5 | 4.5 | 4.5 | 4.4 | 1037 | 1029 | 1029 | 1000 |
| 5 | 1167 | 4.5 | 4.5 | 4.5 | 3.6 | 2382 | 2361 | 2364 | 1800 |
| 6 | 1851 | 4.5 | 4.5 | 4.5 | 3.6 | 3780 | 3745 | 3751 | 2900 |
| 7 | 1545 | 4.5 | 4.5 | 4.5 | 3.7 | 3154 | 3130 | 3127 | 2500 |
| 8 | 1026 | 4.5 | 4.5 | 4.5 | 3.6 | 2095 | 2076 | 2076 | 1600 |
| 9 | 884 | 4.5 | 4.5 | 4.5 | 4.7 | 1804 | 1787 | 1788 | 1900 |
| 10 | 1346 | 4.5 | 4.5 | 4.5 | 4.6 | 2747 | 2720 | 2723 | 2200 |
| 11 | 1584 | 4.5 | 4.5 | 4.5 | 3.8 | 3233 | 3206 | 3204 | 2600 |
| 12 | 1227 | 4.5 | 4.5 | 4.5 | 3.8 | 2504 | 2483 | 2483 | 2000 |
| 13 | 752 | 4.5 | 4.5 | 4.5 | 3.7 | 1535 | 1522 | 1521 | 1200 |
| 14 | 868 | 4.5 | 4.5 | 4.5 | 4.2 | 1772 | 1753 | 1754 | 1600 |
| 15 | 1584 | 4.5 | 4.5 | 4.5 | 3.8 | 3234 | 3206 | 3206 | 2600 |
| 16 | 1232 | 4.5 | 4.5 | 4.5 | 3.6 | 2516 | 2496 | 2497 | 1900 |
| 17 | 503 | 4.5 | 4.5 | 4.5 | 4.4 | 1027 | 1018 | 1018 | 1000 |
| 18 | 1020 | 4.5 | 4.5 | 4.5 | 3.6 | 2082 | 2064 | 2065 | 1600 |
| 19 | 752 | 4.5 | 4.5 | 4.5 | 3.7 | 1535 | 1522 | 1522 | 1200 |

**Table 7d**
Results of the verifications for the CSSBs.

| | *CSSB type 1* | | *CSSB type 2* | |
|---|---|---|---|---|
| Structure | $(N_{Ed}/N_d)_{max}$ | $(N_{Ed}/N_d)_{min}$ | $(N_{Ed}/N_d)_{max}$ | $(N_{Ed}/N_d)_{min}$ |
| SBI.HC | 0.95 | 0.03 | / | / |
| SBI.HVC | 0.97 | 0.02 | / | / |
| SBI.HD | 0.97 | 0.02 | / | / |
| SBI.HVD | 0.99 | 0.02 | 0.99 | 0.30 |

($N_{Ed}$) as function of the known value of the quasi-permanent gravity loads ($N_{Sd}$) transmitted from the superstructure. Two in-plan configurations of the CSSBs involve: i) nineteen isolators with the same value of $\mu_{fast}$ (i.e. CSSBs type 1 shown in Fig. 7a), exhibiting different values of the radius R for the SBI.HC, SBI.HVC and SBI.HD structures; ii) eight types of CSSBs with a different value of $\mu_{fast}$ for the SBI.HVD structure (Fig. 7b).

For the sake of brevity, two types of CSSBs are presented in Fig. 7b: CSSBs type 1, with $\mu_{fast}$ = 4.2–4.4; CSSBs type 2, with $\mu_{fast}$ = 3.6–3.7. In particular, the dynamic properties of the SBI structures are reported in Table 7a, confirming the effectiveness of the sliding bearings in reducing torsional coupling [23], while the geometric and mechanical properties of the CSSBs are shown in Table 7b. Interestingly, the eccentricities between mass and stiffness centres of the superstructure and base-isolation system, respectively, are less marked for the SBI (see Table 7b) than for the EBI (see Table 7c) structures.

Finally, local design parameters and results of the verifications for CSS bearings are reported in Tables 7c and 7d, respectively. Note that the proportioning of the isolators is influenced by the maximum compressive $(N_{Ed}/N_d)_{max}$ and minimum tensile $(N_{Ed}/N_d)_{min}$ axial loads ratios, $N_d$ being the axial load corresponding to the seismic load combination at the CP limit state.

The restoring force of a CSSB during the sliding phase contains pendular and friction components that can be evaluated by considering the following equation [45]

$$\boldsymbol{F}_H = \begin{Bmatrix} F_{H,x} \\ F_{H,y} \end{Bmatrix} \cong \frac{N}{R} \begin{Bmatrix} u_{H,x} \\ u_{H,y} \end{Bmatrix} + \mu N \frac{1}{\|\dot{u}_H\|} \begin{Bmatrix} \dot{u}_{H,x} \\ \dot{u}_{H,y} \end{Bmatrix} \tag{13}$$

where N is the axial load during an earthquake, producing variations of both the friction force and lateral stiffness in the sliding phase, while $\boldsymbol{u}_H = (u_{H,x}, u_{H,y})^T$ and $\dot{\boldsymbol{u}}_H = (\dot{u}_{H,x}, \dot{u}_{H,y})^T$ are vectors of the horizontal displacement and velocity, respectively. Moreover, a circular interaction domain can be used to represent the biaxial interaction, where the direction of the hysteretic force is controlled by the incremental plastic displacements [46]. Experimental studies have highlighted the presence of many parameters affecting the friction coefficient (μ) at the sliding surface of a CSSB [47]. In order to consider the transition between sliding and sticking phases, a modified expression of the friction coefficient defined as a function of the sliding velocity is adopted [48]

$$\mu = \mu_{fast} - (\mu_{fast} - \mu_{rev}) e^{-\alpha \dot{u}_H} \tag{14}$$

replacing the dynamic-slow friction coefficient ($\mu_{slow}$) with the static value at motion reversal ($\mu_{ev}$) and assuming $\mu_{rev}/\mu_{fast} \cong 2$ and $\alpha$ = 0.1 s/mm. Furthermore, the CSS bearing does not resist tensile axial loads and is thus free to uplift. A gap element with infinitely rigid behaviour in compression is assumed in the vertical direction, to account for the fact that the reversal of the axial load from compression to tension is possible

$$F_V = N \text{ for} u_V \geq 0 \text{ and } F_V = 0 \text{ for } u_V < 0 \tag{15}$$

where $u_V$ is the vertical displacement and the equivalent viscous damping in the vertical direction is neglected.

## 5. Numerical results

Nonlinear dynamic analysis of the in-plan irregular r.c. framed structure described in Section 3, before (i.e. fixed-base configuration, FB) and after (i.e. base-isolated configuration, BI) retrofitting with elastomeric (EBI) and sliding (SBI) bearings, is carried out to evaluate seismic demand induced by pulse- and non-pulse-type near-fault earthquakes. Specifically, in the design of the seismic isolation system the horizontal seismic loads are considered to act alone (EBI.H and SBI.H structures) or in combination with the vertical ones (EBI.HV and SBI.HV structures), assuming both moderately-soft (i.e. subsoil class C) and soft (i.e. subsoil class D) sites. A lumped plasticity model with hardening ratio p = 5%, comprising linearly elastic and elastic-perfectly plastic elements acting in parallel, is used to describe the inelastic behaviour of the r.c. frame members of the superstructure [49]. The interaction between axial load (N) and biaxial bending moment ($M_y$-$M_z$) is taken into account by a piecewise linearization of the elastic domain. In detail, 26 flat surfaces are considered as an acceptable compromise between accuracy and computational efficiency, including: 6 surfaces normal to the principal axes; 12 surfaces normal to the

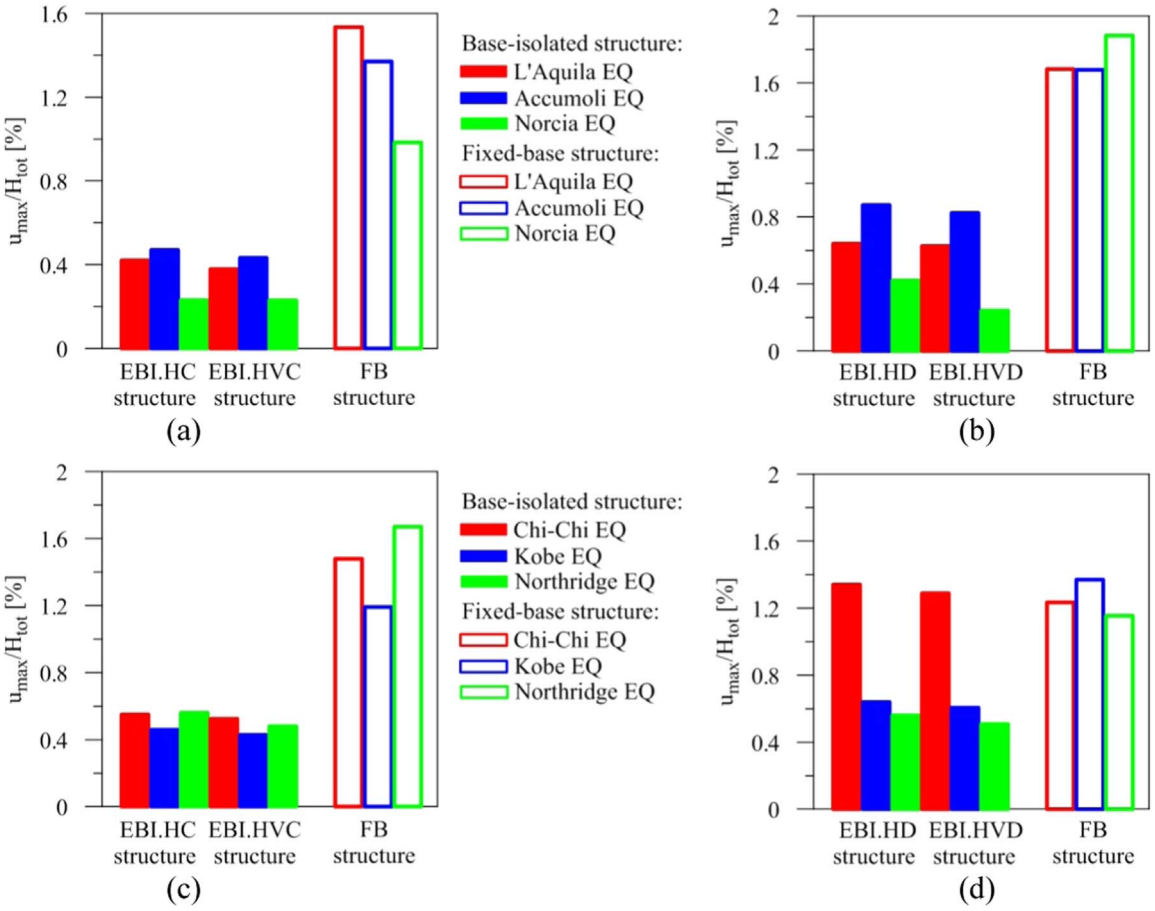


**Fig. 8.** Roof drift ratio of the original FB and retrofitted EBI structures subjected to near-fault earthquakes in central Italy (a, b) and worldwide (c, d).

bisections of the principal planes; 8 surfaces normal to the bisections of the octants. At each critical end-section of a frame member, the elastic-plastic solution referring to the *k-th* flat surface is the one at a minimum distance from the elastic solution, in terms of complementary energy. Then, a viscous damping ratio equal to 1% is considered with reference to the two vibration periods corresponding to high-participation modes with components prevailing in the horizontal direction. Finally, the nonlinear force-displacement laws described in Section 4 are adopted to include coupled bi-directional motions in horizontal directions and coupling of vertical and horizontal motions for both HDLRBs (Section 4.1) and CSSBs (Section 4.2). It should be noted that all earthquakes are first normalized by scaling their PGA values with reference to the MVSI values provided by NTC08 at the CP limit state.

Firstly, the total structural damage to the original FB and retrofitted EBI structures is reported in Fig. 8, considering earthquakes in central Italy (Fig. 8a, b) and worldwide (Fig. 8c, d) for moderately-soft (Fig. 8a, c) and soft (Fig. 8b, d) near-fault sites. It is evaluated in terms of the maximum roof drift ratio, defined as the ratio of the peak horizontal roof displacement ($u_{max}$) to the building height ($H_{tot}$), which correlates with the overall structural damage [50]. In particular, horizontal displacement and height of the base isolation system are deducted from $u_{max}$ and $H_{tot}$, respectively, in the case of the EBI structures. Maximum values from those separately obtained for different recording stations are considered for the Italian earthquakes. Moreover, four orientations of the building plan are examined for all test structures with reference to the orientation of each recording station. Results reported in Fig. 8a, c highlight the fact that the EBI.HC and EBI.HVC retrofitted structures work better than the original FB structure for moderately-soft soil, with a mean reduction of the roof drift ratio of about 70%. An increase in global structural demand is observed for the EBI.HD and EBI.HVD retrofitted structures subjected to the pulse-type Italian EQs (i.e. the L'Aquila and Accumoli EQs) unlike the Norcia site which has experienced non-pulse-type EQs (Fig. 8b). On the other hand, the most detrimental worldwide are obtained for the Chi-Chi EQ (Fig. 8d), exhibiting markedly higher values of the pulse indicator than those observed for the Northridge and Kobe EQs.

Next, the storey damage of the original FB and retrofitted EBI structures is shown in Figs. 9 and 10 for near-fault earthquakes in central Italy and worldwide, respectively, to identify weak storeys. In particular, the maximum interstorey drift ratio $(\Delta/h)_{max}$, defined as drift ($\Delta$) normalized by the storey height (h), is plotted for all storeys of the superstructure. The drift ratio thresholds related to various damage levels of r.c. elements, in the case of ductile structural systems, are also reported [51].

As shown, the original FB structure suffers severe damage with an irregular vertical distribution characterized by maximum values at the lower levels. The insertion of the HDLRBs spreads the storey drift more evenly for subsoil class C (Fig. 9a, b and Fig. 10a, b), reducing the values in the range of moderate ($0.4 < (\Delta/h)_{max} < 1$) and light ($0.2 < (\Delta/h)_{max} < 0.4$) damage at lower and higher levels, respectively. In some cases, irreparable and severe damage is observed in central Italy (Fig. 9c, d) and worldwide (Fig. 10c, d), respectively, when subsoil class D is considered. Similar values of $(\Delta/h)_{max}$ are obtained for the EBI structures subjected to the L'Aquila and Accumoli EQs (Fig. 9), which are characterized by comparable values of the pulse indicator, while less (repairable) damage is observed for the Norcia EQs classified as non-pulse-type records. A good correlation between values of the storey damage and pulse indicator is also confirmed for the EQs worldwide (Fig. 10), among which the Chi-Chi EQs confirms the highest potential of structural damage. Finally, similar results are obtained for the base-

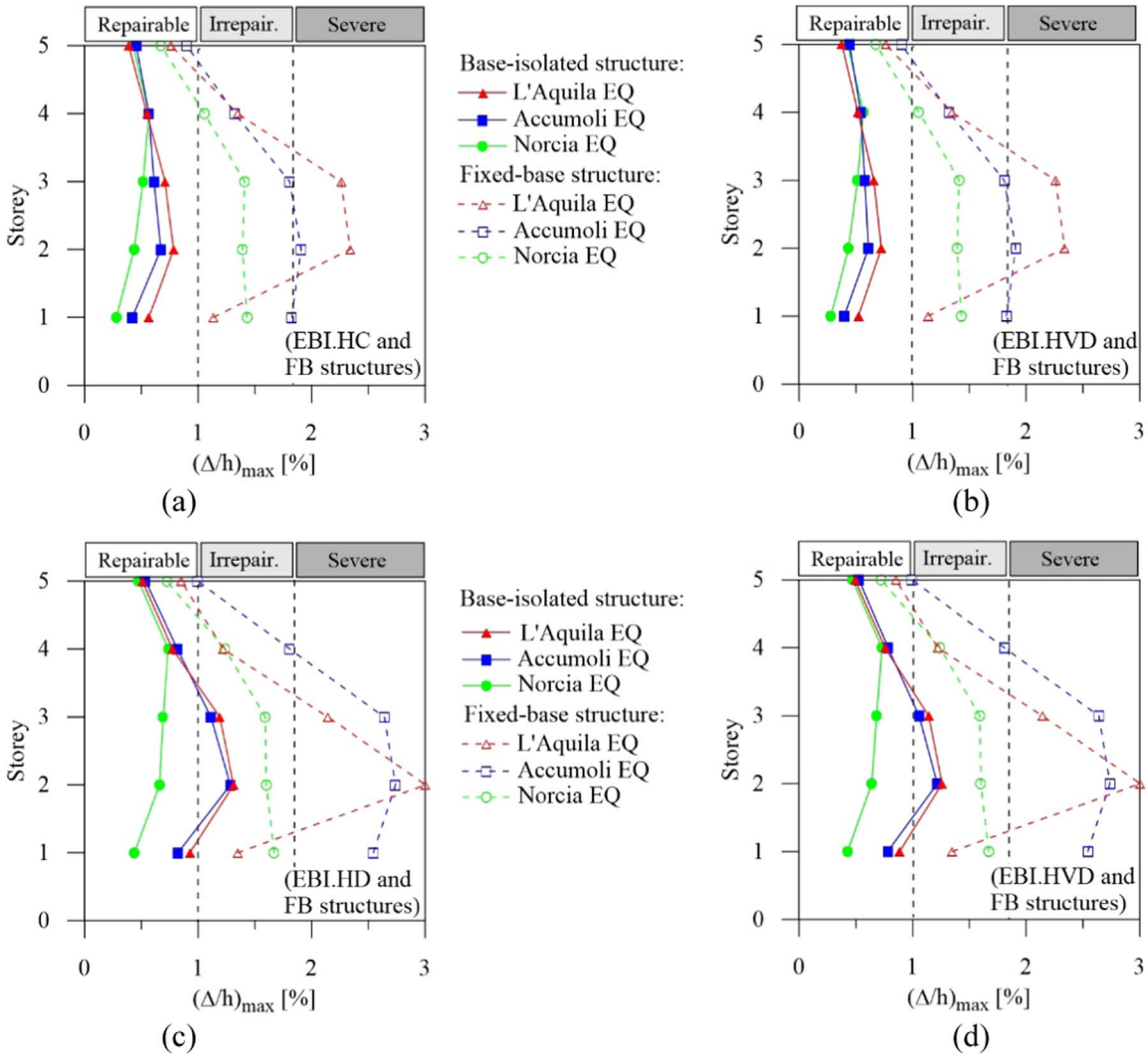


**Fig. 9.** Interstorey drift ratio of the original FB and retrofitted EBI structures subjected to near-fault earthquakes in central Italy.

isolated structures retrofitted considering the horizontal seismic loads acting alone (i.e. the EBI.HC and EBI.HD structures) or in combinations with the vertical ones (i.e. the EBI.HVC and EBI.HVD structures).

Further results, omitted for brevity, highlight that the pulse-type nature of near-fault ground motions can induce unexpected ductility demands at the end sections of beams, especially in the lower storeys. As regards the columns, the addition of the vertical motion induced variation of the axial load, producing even tension or a compressive load larger than the balanced load.

Afterwards, maximum in-plan drift ratio $(\Delta_p/L)_{max}$, evaluated as the in-plan relative displacement ($\Delta_p$) divided by the length (L) of the building plan, is plotted in Fig. 11 for the original (FB) and retrofitted (EBI.HVC and EBI.HVD) test structures subjected to the near-fault earthquakes in Italy (Fig. 11a, b) and worldwide (Fig. 11c, d).

In particular, the relative displacements is evaluated as

$$d_X(t) = u_{X,1}(t) - u_{X,17}(t),\ d_Y(t) = u_{Y,1}(t) - u_{Y,4}(t) \tag{16a,b}$$

referring to the displacement time history of three corners of the building plan (i.e. corners 1, 4 and 17 shown in Fig. 5a). Then, the in-plan drift ratio, which is an indicator of the floor displacement due to torsion, is represented by

$$\Delta_p(t) = d_X(t)/L_Y = d_Y(t)/L_X \tag{17}$$

with a maximum absolute value

$$(\Delta_p/L)_{max} = \max\{|\Delta_p(t)|\},\ t = 0{-}t_{tot} \tag{18}$$

where $L_X$ and $L_Y$ represent the maximum length of the building plan along the X and Y directions and $t_{tot}$ is the total duration of the earthquake.

For the torsionally stiff FB structure (see Table 5b), only limited floor rotations are obtained, whose values increase along the building height but are not correlated with the subsoil class and the pulse indicator characterizing each near-fault earthquake. Moreover, the selected earthquakes do not lead to significant torsional motions of the retrofitted buildings, so the overall responses of the base-isolation system and superstructure are mainly governed by the lateral response. Such behaviour is in line with the observations of previous studies [22,23], highlighting a reduction of the torsional amplification with decreasing values of the isolation and superstructure eccentricities and increasing values of the superstructure and base ratios of torsional-to-lateral frequencies.

Correlation between seismic response of the base-isolated structures and pulse-type intensity of the selected (scaled) near-fault earthquakes is reported in Fig. 12. In particular, global (i.e. maximum roof drift ratio, $u_{max}/H_{tot}$) and local (i.e. in-elevation $(\Delta/h)_{max}$ and in-plan $(\Delta_p/h)_{max}$ drift ratios) engineering demand parameters (EDPs) of the EBI.HVC and EBI.HVD structures are related to the pulse indicator (PI) values reported in Tables 4a and 4b for near-fault EQs in central Italy and worldwide, respectively. Preliminarily, it should be noted that the

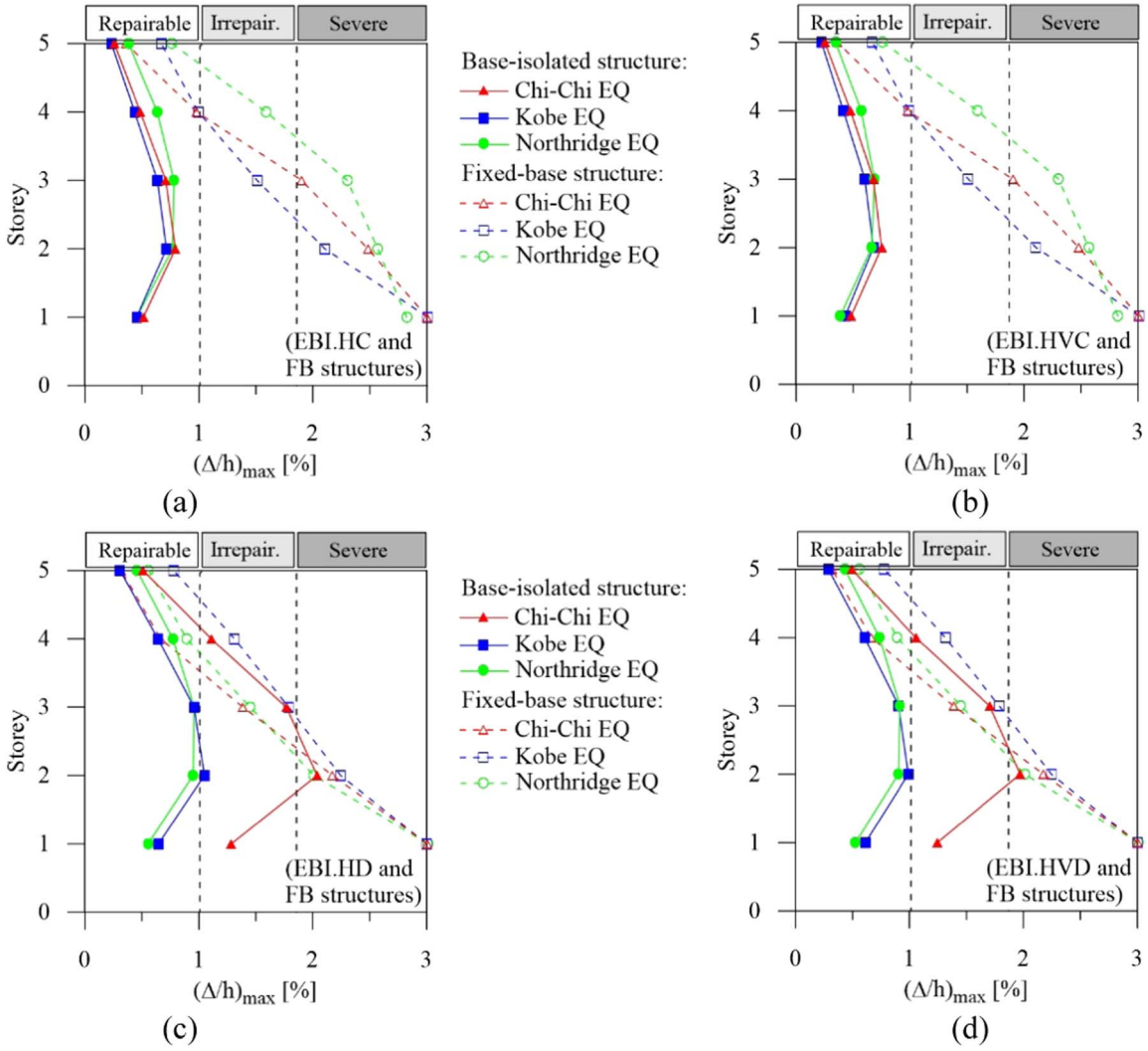


**Fig. 10.** Interstorey drift ratio of the original FB and retrofitted EBI structures subjected to near-fault earthquakes worldwide.

EDP-PI relationships follow a standard linear regression. To find out how well linear regression fits the cloud of data, the coefficient of correlation (r) is evaluated, which is a measure of how close the data are to the regression line (r values close to one indicate a very good correlation). As can be observed, roof (Fig. 12a) and in-elevation (Fig. 12b) drift ratios highlight a good correlation with PI values, especially for soft-soil site (i.e. subsoil class D). On the other hand, in-plan drift ratio (Fig. 12c) has a weak correlation with PI values, exhibiting a wide dispersion of the cloud regression for both moderately soft- and soft-site.

Further results, omitted for the sake of brevity, confirm limited values of tensile stress and compression axial load for the elastomeric isolators of all the examined cases; moreover, maximum shear strains $\gamma_{tot,max} \leq 5$ and $\gamma_{s,max} \leq 2$ are also obtained.

Then, nonlinear dynamic analyses of the retrofitted SBI.H and SBI.HV structures subjected to near-fault earthquakes in central Italy (Tables 8a and 8b) and worldwide (Tables 8c and 8d) are carried out. Unlike the EBI structures, the response of the SBI structures is strongly affected by the CSSBs bearings whose inability to withstand tensile loads and critical behaviour under extreme compressive loads cause rocking and rupture, respectively, compromising their capacity to support the vertical load. It should be noted that seismic verification of the CSSBs at the collapse prevention limit state was always satisfied (see Table 7d). In fact, all the analyses terminate before the end of the ground motion because of uplift (i.e. $N < 0$) and/or because axial load capacity is attained (i.e. $|N| > N_{Ed}$) for some CSSBs, whose position in the building plan is reported in Tables 7a and 7d. (Tables 8c and 8d)

Certainly, the overturning moment produced by the horizontal components of near-fault ground motions and in-plan irregularity contribute to tensile axial forces in the corner bearings. Moreover, perimeter and interior bearings are frequently subjected to large compressive axial forces because their tributary mass is greater than that of a corner bearing. As can be observed, there is a weak correlation between pulse indicator (PI) and axial force (N) defining the collapse limit state of the CSSBs, also because high values of the ratio between vertical and horizontal peak ground acceleration characterize some near-fault ground motions with lower PI value (e.g. Northridge EQ). Moreover, further studies are necessary to evaluate an efficient intensity measure able to predict engineering demand parameters of base-isolated structures subjected to near-fault earthquakes with a significant vertical component. Next, maximum interstorey drift ratio produced by pulse-type near-fault earthquakes recorded or rotated in line with the orientation of the strongest potential pulse derived from the wavelet analysis (see Section 2) are plotted in Fig. 13, referring to the EBI.HVC (Fig. 13a, c) and EBI.HVD (Fig. 13b, d) base-isolated structures. Specifically, four orientations of the building plan are examined for both recorded and rotated horizontal components of near-fault earthquakes in central Italy (Fig. 13a, b) and worldwide (Fig. 13c, d). It is worth noting that $(\Delta/h)_{max}$ values for the rotated earthquakes are generally greater than those obtained for the recorded ones, especially for

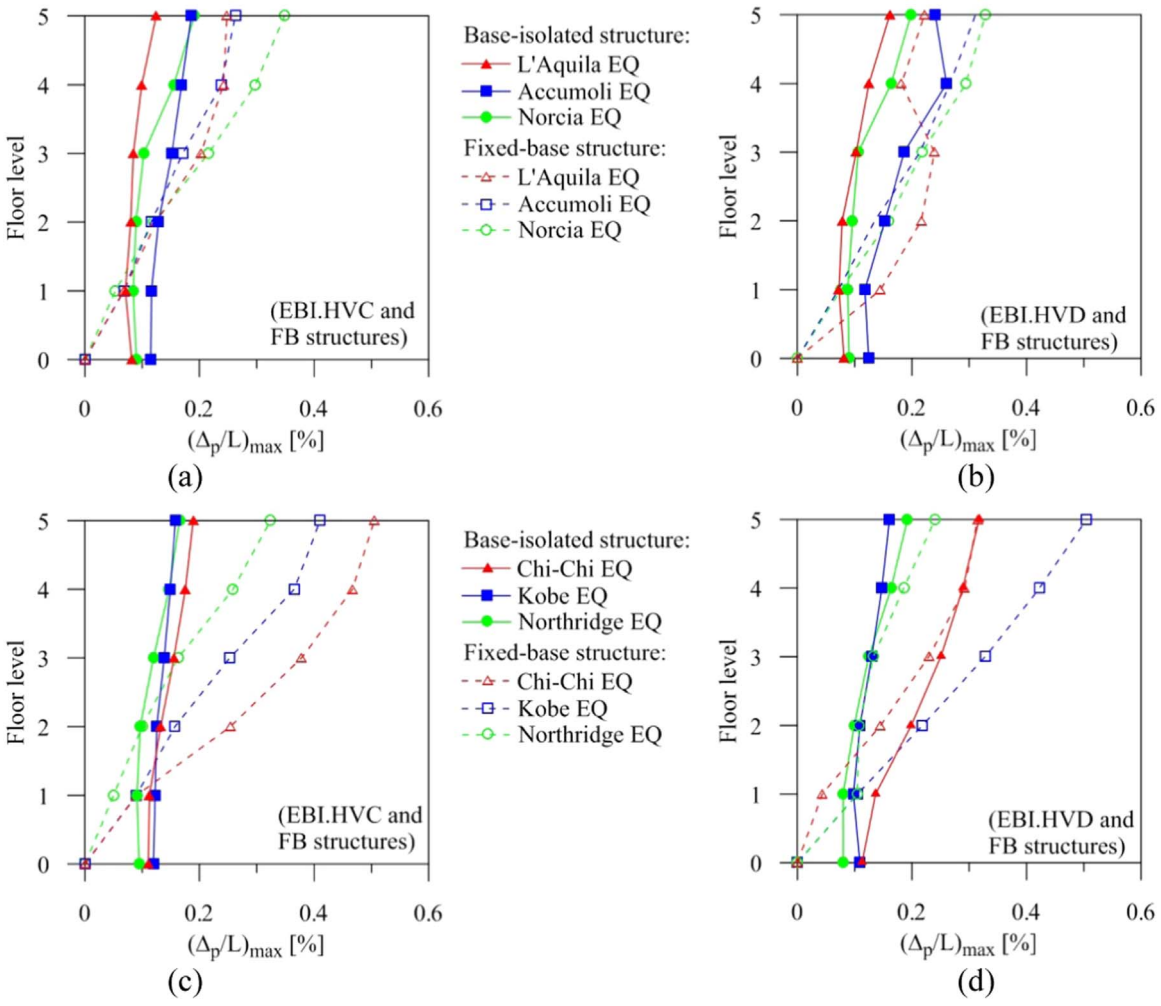


**Fig. 11.** In-plan drift ratio of the original FB and retrofitted EBI structures subjected to near-fault earthquakes in central Italy and worldwide.

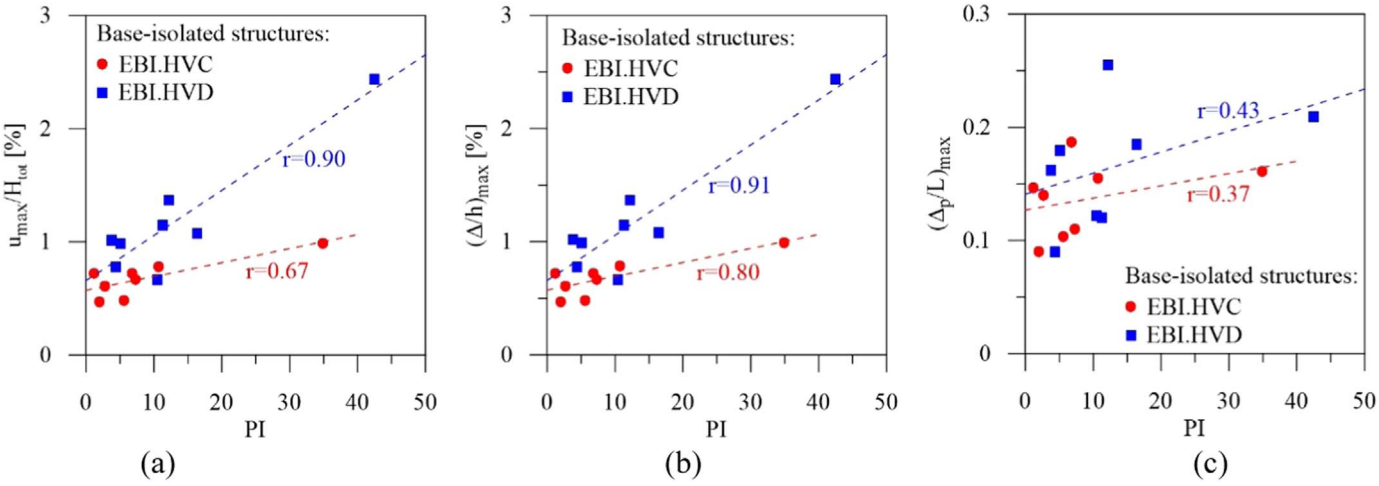


**Fig. 12.** Correlation between seismic demand parameters of the base-isolated structures and pulse indicator (PI) of the near-fault EQs.

increasing values of PI and subsoil class D (Fig. 13b, d). Further results, omitted for the sake of brevity, confirm this trend also with reference to curvature ductility demand of beams and columns. Graphs similar to the previous ones are reported in Fig. 14, where attention is focused on $(\Delta/h)_{max}$ values corresponding to the L'Aquila EQs recorded at different stations, placed at close range to one another but producing significant variations in the PI values (see Table 4a). As can be observed, the interstorey drift ratios of the EBI.HVD structure (Fig. 14b) corresponding to the AQK station are much greater than those observed for the AQG station, confirming a good correlation between the PI value and seismic demand.

Finally, the influence of pulse-type and non-pulse-type near-fault earthquakes on the accrual of residual displacements, during aftershocks or after a sequence of seismic events, are investigated in Fig. 15.

**Table 8a**
Results for retrofitted SBI structures on moderately soft soil subjected to near-fault earthquakes in central Italy.

| *Earthquake (EQ)* | *Recording station* | *SBI.HC* | | | *SBI.HVC* | | |
|---|---|---|---|---|---|---|---|
| | | *t* [s] | *CSSBs with* $\|N\| > N_{Ed}$ | *CSSBs with* $N < 0$ | *t* [s] | *CSSBs with* $\|N\| > N_{Ed}$ | *CSSBs with* $N < 0$ |
| L'Aquila | AQV | 2.254 | 3, 14, 16 | – | 2.253 | 3, 14 | – |
| | AQG | 3.126 | 3 | 1, 17 | 3.126 | 3 | 1 |
| | AQA | 2.859 | – | 17 | 2.859 | – | 17 |
| | AQK | 2.881 | – | 1 | 2.888 | – | 1 |
| Accumoli (Rieti) | AMT | 2.577 | – | 1 | 2.576 | – | 1 |
| | NRC | 3.950 | 3 | – | 3.951 | 3 | – |
| | NOR | 4.052 | – | 1 | 4.052 | – | 1 |
| | FEMA | 4.920 | 3 | – | 4.918 | 3 | – |
| Norcia (Rieti) | FCC | 2.110 | – | 2 | 2.110 | – | 2 |
| | NOR | 3.303 | 12, 16 | – | 3.218 | 12, 16 | – |

**Table 8b**
Results for retrofitted SBI structures on soft soil subjected to near-fault earthquakes in central Italy.

| *Earthquake (EQ)* | *Recording station* | *SBI.HD* | | | *SBI.HVD* | | |
|---|---|---|---|---|---|---|---|
| | | *t* [s] | *CSSBs with* $\|N\| > N_{Ed}$ | *CSSBs with* $N < 0$ | *t* [s] | *CSSBs with* $\|N\| > N_{Ed}$ | *CSSBs with* $N < 0$ |
| L'Aquila | AQV | 2.251 | 3, 14 | – | 2.000 | 16 | – |
| | AQG | 2.998 | 3 | 17 | 2.204 | 12 | – |
| | AQA | 2.673 | – | 17 | 2.272 | 7, 12, 16 | – |
| | AQK | 2.887 | – | 1 | 1.802 | 3 | – |
| Accumoli (Rieti) | AMT | 2.573 | – | 1 | 2.404 | 12, 16 | – |
| | NRC | 3.952 | 3 | – | 2.948 | 12, 16 | – |
| | NOR | 4.060 | – | 1 | 4.074 | 3, 5 12, 16 | 1 |
| | FEMA | 4.915 | 3 | – | 3.916 | 12 | – |
| Norcia (Rieti) | FCC | 3.351 | 12 | – | 1.200 | 16 | – |
| | NOR | 3.209 | 16 | – | 2.943 | 16 | – |

**Table 8c**
Results for retrofitted SBI structures on moderately-soft soil subjected to near-fault earthquakes worldwide.

| *Earthquake (EQ)* | *Recording station* | *SBI.HC* | | | *SBI.HVC* | | |
|---|---|---|---|---|---|---|---|
| | | *t* [s] | *CSSBs with* $\|N\| > N_{Ed}$ | *CSSBs with* $N < 0$ | *t* [s] | *CSSBs with* $\|N\| > N_{Ed}$ | *CSSBs with* $N < 0$ |
| Chi-Chi (Taiwan) | TCU068 | 9.388 | 9, 12, 14 | 2 | 9.388 | 9, 12, 14 | – |
| Northridge (California) | Rinaldi Rec. Stat. | 0.831 | – | 10 | 0.831 | – | 10 |
| Kobe (Japan) | Takatori | 2.242 | 12 | 4 | 2.243 | 12 | 4 |

**Table 8d**
Results for retrofitted SBI structures on soft soil subjected to near-fault earthquakes worldwide.

| *Earthquake (EQ)* | *Recording station* | *SBI.HD* | | | *SBI.HVD* | | |
|---|---|---|---|---|---|---|---|
| | | *t* [s] | *CSSBs with* $\|N\| > N_{Ed}$ | *CSSBs with* $N < 0$ | *t* [s] | *CSSBs with* $\|N\| > N_{Ed}$ | *CSSBs with* $N < 0$ |
| Chi-Chi (Taiwan) | TCU068 | 9.379 | 9, 12 | – | 9.146 | 12 | – |
| Northridge (California) | Rinaldi Rec. Stat. | 0.831 | – | 10 | 0.656 | 16 | – |
| Kobe (Japan) | Takatori | 1.679 | 12 | – | 1.569 | 12, 16 | – |

More specifically, maximum values of the roof (Fig. 15a) and interstorey (Fig. 15b) drift ratios are evaluated for the original FB and retrofitted EBI.HVC and EBI.HVD structures. Nonlinear dynamic analyses are carried out to consider a real sequence of an Italian near-fault earthquake characterized by one main-shock (October 26th, 2016) and one aftershock (October 30th, 2016) recorded by the same station (i.e. the NOR station shown in Table 1a). Note that residual displacements tend towards higher values in the case of the original FB structure, especially for soft-soil site, with the exception of the first storey where a subtraction or residual displacement is observed when another earthquake occurs. On the other hand, permanent displacements reverse and become almost zero at the end of the second sequence in the case of base-isolation with elastomeric bearings, confirming their effectiveness in preventing the accumulation of roof drift and interstorey drift ratios for both moderately-soft and soft subsoil classes. However, before any firm conclusion is drawn, a considerable number of real sequences of seismic records need to be assessed to obtain a better understanding of this phenomenon.

## 6. Conclusions

This work has studied the effectiveness of base-isolation with elastomeric (i.e. HDLRBs) and sliding (i.e. CSSBs) bearings for the seismic retrofitting of r.c. irregular framed buildings, with regard to pulse-type and non-pulse-type ground motions and different site conditions in the near-fault area. To this end, a simulation is conducted in which a five-storey reinforced concrete (r.c.) benchmark structure of the Re.L.U.I.S. project, characterized by an asymmetric-plan and irregularity due to

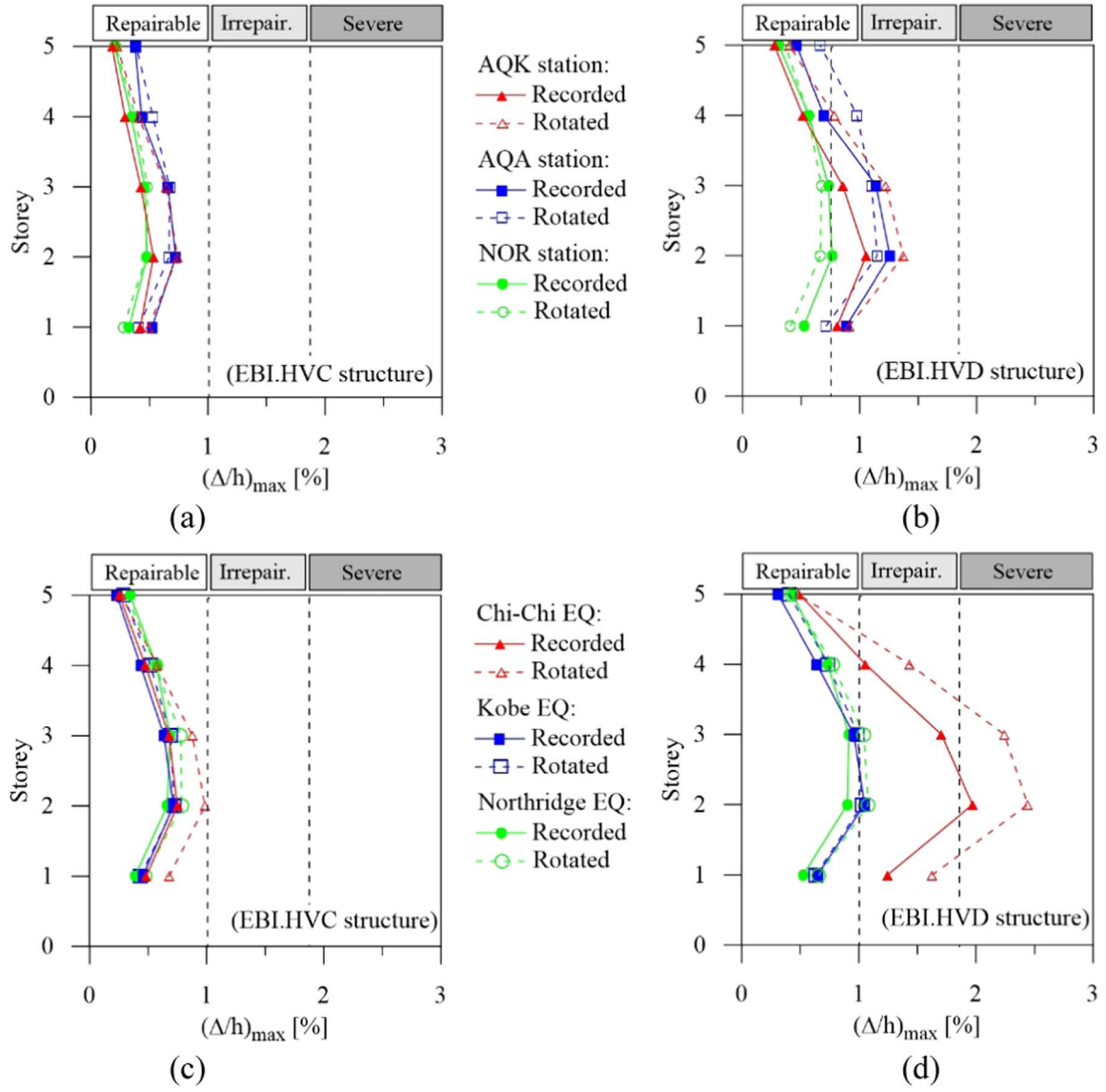


**Fig. 13.** Interstorey drift ratio of the retrofitted EBI structures for recorded and potential pulse orientations of near-fault earthquakes in central Italy and worldwide.

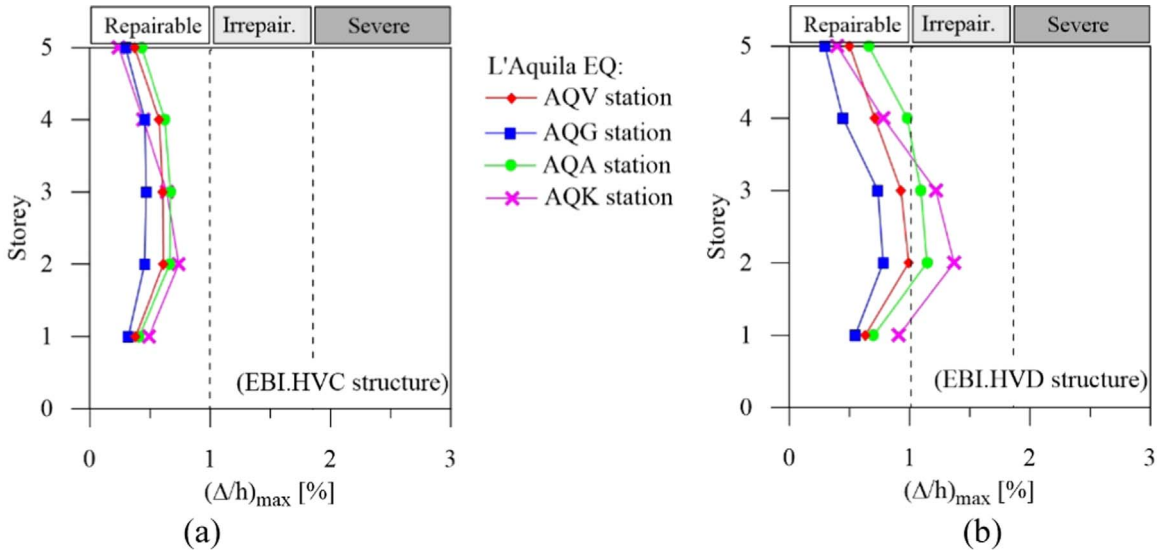


**Fig. 14.** Interstorey drift ratio of the retrofitted EBI structures subjected to the near-fault L'Aquila earthquakes recorded at different stations.

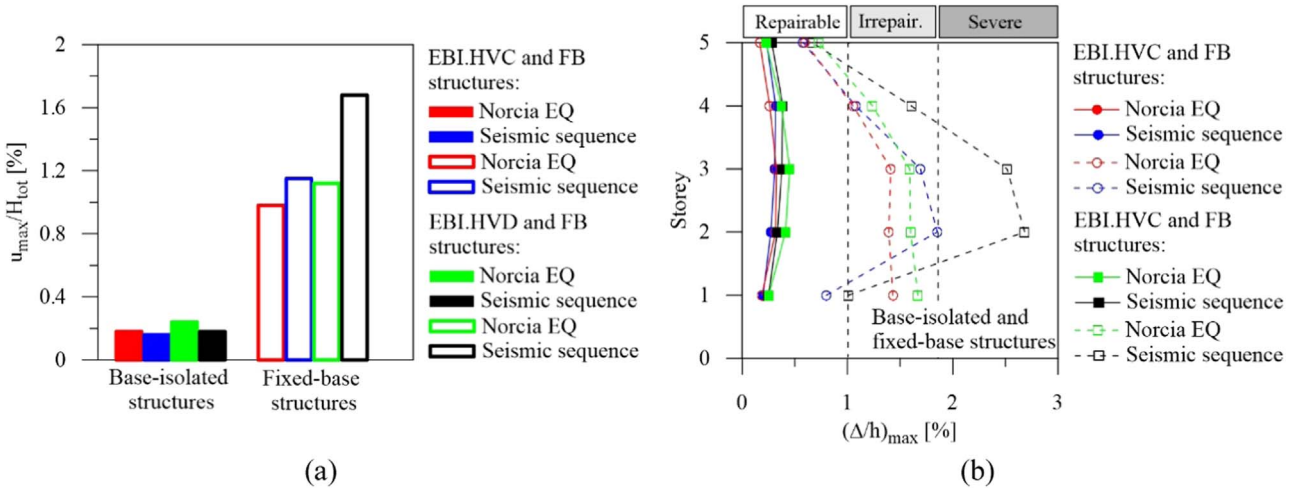


**Fig. 15.** Effects of the residual displacements of the original FB and retrofitted EBI structures subjected to the near-fault Norcia earthquakes recorded in sequence at the same station.

bays of different length, is retrofitted with regard to four structural solutions for each base-isolation system, diversified assuming two in-plan distributions of HDLRBs and CSSBs and moderately-soft and soft subsoil conditions. The records of near-fault earthquakes in recent central Italy and worldwide have been selected and continuous wavelet transforms of the two horizontal components used to identify all the orientations most likely to contain a pulse, in terms of a predictor of the likelihood that a given record is pulse-type.

With the wavelet analyses, false-negative classifications occur when only fault-normal pulse direction is adopted. Specifically, polar plots of a pulse indicator (PI) confirm pulses around this orientation for the L'Aquila and Accumoli EQs, while this orientation does not lie within the range in which pulses are observed for the Ussita EQ. Similarly, in the Kobe EQ pulses are predominant perpendicular to the fault, unlike the Taiwan and Northridge EQs where pulses deviate from the fault-normal orientation. On the other hand, false-positive classifications of pulses are removed due to a change in the PGV threshold. This happened for the L'Aquila (AQV and AQG stations), Accumoli (AMT, NRC and FEMA stations) and Ussita (NOR station) near-fault ground motions, while worldwide the potential pulses of the near-fault EQs exhibit markedly higher values of the pulse indicator than those obtained for the EQs in central Italy.

The results of the nonlinear dynamic analysis highlight that the original torsionally stiff FB structure suffers severe global and local damage, with an irregular vertical distribution characterized by maximum values at the lower levels, while only limited floor rotations are resulted. The retrofitted EBI.HC and EBI.HVC structures present more uniform distribution of the storey drift, reducing the values to within the range of moderate and light damage at lower and higher levels, respectively. Irreparable and severe damage is observed in central Italy and worldwide, respectively, when the EBI.HD and EBI.HVD structures are examined. However, the selected earthquakes do not cause significant torsional motions to the retrofitted base-isolated buildings, hence the responses of the HDLRBs and superstructure are mainly governed by the lateral response. It is worth noting that roof and in-elevation drift ratios highlight a good correlation with PI values, especially for soft-soil site. A weak correlation is observed with the in-plan drift ratio, characterized by a considerable dispersion of the cloud regression for both moderately-soft and soft sites. The response of the retrofitted SBI structures is strongly affected by tensile loads and critical behaviour under large compressive loads, producing rocking and rupture, respectively. There is a little correlation between pulse indicator and axial force defining the collapse limit state of the CSSBs in this case. From the wavelet analysis the highest demand parameters are produced by pulse-type near-fault earthquakes rotated in line with the orientation of the strongest potential pulse. Finally, residual displacements tend to increase in the case of the original FB structure subjected to a seismic sequence of near-fault EQs, especially for soft-soil site, while permanent displacements reverse to almost zero at the end of the second sequence in the case of base-isolation with HDLRBs.

Seismic demand of plan-irregular base-isolated structures located in a near-fault area depends on the forward-directivity pulses, especially for soft subsoil class, and the pulse indicator can be used to predict global and local structural damage of the superstructure. Moreover, the above considerations indicate that the effects of pulse-type near-fault ground motions should be taken into account through the adoption of site-specific response spectra. Further studies are needed to extend the analysis to other base-isolated structures and recorded near-fault ground motions, to represent as much as possible expected structural and ground-shaking situations. Finally, an efficient intensity measure for base-isolated structures subjected to near-fault earthquakes with a significant vertical component needs to be developed.

## Acknowledgements

The present work was financed by Re.L.U.I.S. (Italian network of university laboratories of earthquake engineering), in accordance with "Convenzione D.P.C.–Re.L.U.I.S. 2017, Research line PR6, Isolation and Dissipation".

## References

[1] Bertero VV, Mahin SA, Herrera RA. Aseismic design implications of near-fault San Fernando earthquake records. Earthq Eng Struct Dyn 1978;6:31–42.
[2] Sehhati R, Rodriguez-Marek A, ElGawady M, Cofer WF. Effects of near-fault ground motions and equivalent pulses on multi-story structures. Eng Struct 2011;33:767–79.
[3] Liu T, Luan Y, Zhong W. Earthquake responses of clusters of building structures caused by a near-field thrust fault. Soil Dyn Earthq Eng 2012;42:56–70.
[4] Diaferio M, Foti D. Mechanical behavior of buildings subjected to impulsive motions. Bull Earthq Eng 2016;14(3):849–62.
[5] Hall JF, Heaton TH, Halling MW, Wald DJ. Near-source ground motions and its effects on flexible buildings. Earthq Spectra 1995;11:569–605.
[6] Jangid RS, Kelly JM. Base isolation for near-fault motions. Earthq Eng Struct Dyn 2001;30:691–707.
[7] Mazza F, Vulcano A. Nonlinear response of r.c. framed buildings with isolation and supplemental damping at the base subjected to near-fault earthquakes. J Earthq Eng 2009;13(5):690–715.
[8] Mazza F, Mazza M. Nonlinear seismic analysis of irregular r.c. framed buildings base- isolated with friction pendulum system under near-fault excitations. Soil Dyn Earthq Eng 2016;90:299–312.
[9] Mazza F, Vulcano A. Effects of near-fault ground motions on the nonlinear dynamic response of base-isolated r.c. framed buildings. Earthq Eng Struct Dyn 2012;41:211–32.
[10] Mazza F, Mazza M, Vulcano A. Nonlinear response of r.c. framed buildings retrofitted by different base-isolation systems under horizontal and vertical components

of near-fault earthquakes. Earthq Struct 2017;12:135–44.
[11] Ramallo JC, Johnson EA, Spencer BF. “Smart” base isolation systems. J Eng Mech 2002;128(10):1088–99.
[12] Menga N, Foti D, Carbone G. Viscoelastic frictional properties of rubber-layer roller bearings (RLRB) seismic isolators. Meccanica 2017;52(11–12):2807–17.
[13] Chioccarelli E, Iervolino I. Near-source seismic demand and pulse-like records: a discussion for L’Aquila earthquake. Earthq Eng Struct Dyn 2010;39(9):1039–62.
[14] Baker JW. Quantitative classification of near-fault ground motions using wavelet analysis. Bull Seismol Soc Am 2007;97(5):1486–501.
[15] Shahi SK, Baker JW. An empirically calibrated framework for including the effects of near-fault directivity in probabilistic seismic hazard analysis. Bull Seismol Soc Am 2011;101(2):742–55.
[16] Shahi SK, Baker JW. An efficient algorithm to identify strong-velocity pulses in multicomponent ground motions. Bull Seismol Soc Am 2014;104(5):2456–66.
[17] Liossatou E, Fardis MN. Near-fault effects on residual displacements of RC structures. Earthq Eng Struct Dyn 2016;45(9):1391–409.
[18] Zimmaro P, Stewart JP. Engineering reconnaissance following the 2016 M 6.0 central Italy earthquake. Geotechnical extreme events reconnaissance association report no. GEER-050; 2016.
[19] Stewart JP, Lanzo G, Pagliaroli A, Scasserra G, Di Capua G, Peppoloni G, et al. Ground motion recordings from the Mw 6.3 2009 L’Aquila earthquake in Italy and their engineering implications. Earthq Spectra 2012;28:317–45.
[20] Pan TC, Kelly JM. Seismic response of torsionally coupled base isolated structures. Earthq Eng Struct Dyn 1983;11(6):749–70.
[21] Eisenberger M, Rutenberg A. Seismic base isolation of asymmetric shear buildings. Eng Struct 1986;8(1):2–8.
[22] Nagarajaiah S, Reinhorn AM, Constantinou MC. Torsion in base-isolated structures with elastomeric isolation systems. J Struct Eng 1993;119(10):2932–51.
[23] Nagarajaiah S, Reinhorn AM, Constantinou MC. Torsional coupling in sliding base-isolated structures. J Struct Eng 1993;119(1):130–49.
[24] Tena-Colunga A, Escamilla-Cruz JL. Torsional amplifications in asymmetric base-isolated structures. Eng Struct 2007;29(2):237–47.
[25] Tena-Colunga A, Zambrana-Rojas C. Dynamic torsional amplifications of base isolated structures with eccentric isolation system. Eng Struct 2006;28(1):72–83.
[26] Kilar V, Koren D. Seismic behaviour of asymmetric base isolated structures with various distributions of isolators. Eng Struct 2009;31:910–21.
[27] Seguín CE, De la Llera HC, Almazán JL. Base-structure interaction of linearly isolated structures with lateral-torsional coupling. Eng Struct 2008;30(1):110–25.
[28] Ryan KL, Chopra AK. Estimating seismic demands for isolation bearings with building overturning effects. J Struct Eng 2006;132(7):1118–28.
[29] Shen C-Y, Tan P, Cui J, Ma Y-H, Huang X-Y. Critical tension–shear load of elastomeric seismic isolators: an experimental perspective. Eng Struct 2016;121:42–51.
[30] Kasalanati A, Constantinou MC. Testing and modelling of prestressed isolators. J Struct Eng 2005;131(6):857–66.
[31] Tena-Colunga A, Gómez-Soberón C, Muñoz-Loustaunau A. Seismic isolation of buildings subjected to typical subduction earthquake motions for the Mexican Pacific Coast. Earthq Spectra 1997;13(3):505–32.
[32] Tena-Colunga A, Villegas-Jiménez O. The role of modern technologies to safeguard hospitals during earthquakes. In: Proceedings of the 9th US National and 10th Canadian conference on earthquake engineering, reaching beyond borders, Toronto, Canada, paper No. 1705; 2010.
[33] NTC08. Technical regulations for the constructions. Italian Ministry of the Infrastructures; 2008. (D.M. 14-01-2008 and C.M. 2-2-2009).
[34] ITACA. ITalian ACcelerometric archive: a web portal for the dissemination of Italian strong-motion data; 2008. ⟨http://itaca.mi.ingv.it⟩.
[35] PEER. Pacific earthquake engineering research center database; 2008. ⟨http://ngawest2.berkeley.edu⟩.
[36] Baltzopoulos G, Vamvatsikos D, Iervolino I. Analytical modelling of near-source pulse-like seismic demand for multi-linear backbone oscillators. Earthq Eng Struct Dyn 2016;45(11):1797–815.
[37] Somerville PG, Smith NF, Graves RW, Abrahamson NA. Modification of empirical strong motion attenuation relations to include the amplitude and duration effect of rupture directivity. Seismol Res Lett 1997;68(1):199–222.
[38] Iervolino I, Baltzopoulos G, Chioccarelli E. Preliminary engineering analysis of the August 24th 2016, ML 6.0 central Italy earthquake records. Ann Geophys 2016;59:1–9.
[39] Mazza F, Labernarda R. Structural and non-structural intensity measures for the assessment of base-isolated structures subjected to pulse-like near-fault earthquakes. Soil Dyn Earthq Eng 2017;96:115–27.
[40] Magliulo G, Maddaloni G, Cosenza E. Static and dynamic nonlinear analysis of plan irregular existing r/c frame buildings. In: Proceedings of the 14th world conference on earthquake engineering, Beijing, China; October 2008. p. 12–17.
[41] DM96. Norme tecniche per le costruzioni in zone sismiche e relative istruzioni. Italian Ministry of Public Works; 1996. (D.M. 16-01-1996 and C.M. 10-04-1997).
[42] Ryan KL, Kelly JK, Chopra AK. Nonlinear model for lead-rubber bearings including axial-load effects. J Eng Mech 2005;131(12):1270–8.
[43] Naeim F, Kelly JM. Design of seismic isolated structures: from theory to practice. New York, U.S.A.: John Wiley & Sons Ltd; 1999.
[44] FIP Industriale S.p.A. Catalogue S04: curved surface sliders. Padov; 2013. ⟨http://www.fipindustriale.it⟩.
[45] Mazza F. Lateral-torsional response of base-isolated buildings with curved surface sliding system subjected to near-fault earthquakes. Mech Syst Signal Process 2017;92:64–85.
[46] Mosqueda G, Whittaker AS, Fenves GL. Characterization and modeling of friction pendulum bearings subjected to multiple components of excitation. J Struct Eng (ASCE) 2004;130(3):433–42.
[47] Kumar M, Whittaker AS, Constantinou MC. Characterizing friction in sliding isolation bearings. Earthq Eng Struct Dyn 2015;44(9):1409–25.
[48] Fagà E, Ceresa P, Nascimbene R, Moratti M, Pavese A. Modelling curved surface sliding bearings with bilinear constitutive law: effects on the response of seismically isolated buildings. Mater Struct 2016;49(6):2179–96.
[49] Mazza F. Modelling and nonlinear static analysis of reinforced concrete framed buildings irregular in plan. Eng Struct 2014;80:98–108.
[50] Donaire-Ávila J, Mollaioli F, Lucchini A, Benavent-Climent A. Intensity measures for the seismic response prediction of mid-rise buildings with hysteretic dampers. Eng Struct 2015;102:278–95.
[51] Ghobarah A. On drift limits associated with different damage levels. In: Proceedings of the international workshop on the performance-based seismic design: concepts and implementation, Bled, Slovenia. PEER 2004/05 1; 2004. p. 321–332.